

## Electron-parking engineering assisted ZnIn<sub>2</sub>S<sub>4</sub>/Mo<sub>2</sub>TiC<sub>2</sub>-Ru photocatalytic hydrogen evolution for efficient solar energy conversion and storage

Qing Xi <sup>a,b</sup>, Jianxin Liu <sup>a,b,\*</sup>, Fangxia Xie <sup>a,b</sup>, Aoqun Jian <sup>c</sup>, Zijun Sun <sup>d</sup>, Aijuan Zhou <sup>a</sup>, Xuan Jian <sup>e</sup>, Xiaochao Zhang <sup>b</sup>, Yawen Wang <sup>b</sup>, Houfen Li <sup>a</sup>, Xiaoming Gao <sup>e</sup>, Jun Ren <sup>b</sup>, Caimei Fan <sup>a,b</sup>, Jiancheng Wang <sup>a,b,\*</sup>, Rui Li <sup>a,b,\*</sup>

<sup>a</sup> Shanxi Key Laboratory of Compound Air Pollutants Identification and Control, College of Environmental Science and Engineering, Taiyuan University of Technology, Taiyuan 030024, PR China

<sup>b</sup> Key Laboratory of Coal Science and Technology, Ministry of Education, College of Chemical Engineering and Technology, Taiyuan University of Technology, Taiyuan 030024, PR China

<sup>c</sup> Shanxi Key Laboratory of Micro Nano Sensors & Artificial Intelligence Perception, College of Electronic Information and Optical Engineering, Taiyuan University of Technology, Taiyuan 030024, PR China

<sup>d</sup> Xi'an North Huian Chemical Industries Co. Ltd, Xi'an 710302, PR China

<sup>e</sup> College of Chemistry and Chemical Engineering, Shaanxi Key Laboratory of Chemical Reaction Engineering, Yan'an University, Yan'an 716000, PR China



### ARTICLE INFO

#### Keywords:

Photocatalytic hydrogen evolution  
ZnIn<sub>2</sub>S<sub>4</sub>/Mo<sub>2</sub>TiC<sub>2</sub>-Ru  
Electron transfer and storage  
Electron-parking engineering  
Electrons utilization

### ABSTRACT

The electron utilization efficiency in photocatalytic hydrogen evolution (PHE) is crucial for solar energy conversion and storage. Prolonged lifetime and effective use of accumulated electrons based on the storage-release behavior is a potential strategy to regulate the electronic utilization efficiency. Herein, this study utilized Mo<sub>2</sub>TiC<sub>2</sub>-Ru as the “electron-parking” to construct a ZnIn<sub>2</sub>S<sub>4</sub>/Mo<sub>2</sub>TiC<sub>2</sub>-Ru photocatalyst. The ZnIn<sub>2</sub>S<sub>4</sub>/Mo<sub>2</sub>TiC<sub>2</sub>-Ru exhibits a visible light-driven PHE rate of 5.72 mmol·g<sup>-1</sup>·h<sup>-1</sup>, and maintains a PHE rate of ~1.67 mmol·g<sup>-1</sup>·h<sup>-1</sup> under dark conditions. The photogenerated electrons could be directionally stored in Mo<sub>2</sub>TiC<sub>2</sub>-Ru to create an electron-rich environment, this can inhibit backflow and recombination of electrons, and could regulate the water dissociation and hydrogen adsorption kinetics. Importantly, the stored electrons could release in the dark, increasing the quantity of electrons and overcoming intermittent sunlight and regional environmental influences. This work provides insights and references for the development of capacitive co-catalysts with an “electron-parking” engineering for efficient and sustained PHE reactions.

### 1. Introduction

Photocatalytic hydrogen evolution (PHE) technology is an effective sustainable strategy to alleviate the energy shortage and environmental issues [1]. This technique is generally considered to involve three crucial steps: light harvesting to create energetic electrons and holes, charge separation and transfer, and surface redox reactions, all of which are related to the utilization efficiency of electrons [2]. Specifically, the generation of electrons could impact the quantity available for reactions, but is limited by intermittent solar energy at temporal and spatial scales [3]. Furthermore, the separation and transfer of charge determine the efficiency of subsequent surface redox reactions, which is hampered by severe carrier recombination [4]. Therefore, constructing

functional catalysts to achieve high electron utilization through continuous supply and rapid separation is essential for sustainable and efficient PHE process.

Recent studies have shown that the transfer of photogenerated charges occurs on the picosecond (ps) to nanosecond (ns) timescale, while the reduction reactions of electrons take place on timescales ranging from microseconds ( $\mu$ s) to milliseconds (ms) [5]. That is to say, the sluggish reaction kinetics inevitably leads to the accumulation of photogenerated electrons, if without any kind of guidance, these accumulated electrons will flow back to the bulk and recombine with holes, and then reducing the electron utilization efficiency, which serving as the rate-determining step of overall PHE chemical reaction [6]. However, if these accumulated electrons could be stored to form an

\* Corresponding authors at: Shanxi Key Laboratory of Compound Air Pollutants Identification and Control, College of Environmental Science and Engineering, Taiyuan University of Technology, Taiyuan 030024, PR China.

E-mail addresses: liujx0519@163.com (J. Liu), wangjiancheng@tyut.edu.cn (J. Wang), lirui13233699182@163.com (R. Li).

electron-rich environment, and then release them in electron-deficient environment to improve the electron utilization efficiency. In one aspect, the electron-rich environment could accelerate the separation and transfer of electrons under the sunlight irradiation by inhibiting electron backflow, and optimizing the kinetics of surface reduction reactions [7]. In the other aspect, by storing the photogenerated electrons and then releasing the electrons to the PHE reaction, the sustained photoelectrons supply effect will be exerted even after light off, ultimately achieving significantly improved electron utilization efficiencies [8]. Therefore, designing a photocatalyst with electron storage-release characteristics, namely “electron-parking engineering”, is crucial to achieve continuous supply, rapid separation and transfer of electrons.

Inspired by a variety of energy storage materials sprung up, two-dimensional (2D) transition metal carbides MXene is one of the potential candidates due to the 2D structure, metallic conductivity, and abundant surface terminal groups [9]. Specifically, the unique 2D structure and metallic conductivity provide a suitable “platform” for electron transfer [10]. The oxidation state changes of surface metals such as Mo and Ti, and protonation of terminal groups ( $T_x$  with -O to -OH) could serve as an ideal “storage site” for electrons [11]. The isoenergetic charge transfer mechanism demonstrates that photogenerated electrons stored in the form of photoredox chemicals could experience minimal loss of photoelectron redox potential in charge accumulation [3]. However, the storage capacity of electrons in MXene is always limited by its poor in-plane electrical conductivity, stemming from the material’s anisotropy [12]. Ruthenium (Ru) doping has been reported to enhance the capacitance of 2D materials by facilitating in-plane electron transfer and storage, owing to its high electrical conductivity and excellent rate performance [13]. Meanwhile, the nanoparticle-sheet structure of MXene loaded with Ru nanoparticles (NPs) could increase the active sites on the basal plane and provide a low-resistance pathway for accelerating electronic diffusion, thereby facilitating electrons storage and release [14]. Therefore, MXene-Ru should be a suitable substrate for in situ construction of electron-parking photocatalyst systems. Nevertheless, its application for manipulating photoelectron storage-release behavior has yet to be reported.

At last, designing electron-storage photocatalyst also requires a host semiconductor to provide photogenerated electrons. ZnIn<sub>2</sub>S<sub>4</sub> photocatalyst (ZIS) has attracted considerable attention in the field of PHE due to its excellent visible light responsiveness, tunable band gap, low toxicity, and high stability [15]. Previous studies have confirmed that the construction of ZnIn<sub>2</sub>S<sub>4</sub>/MXene Schottky junctions, such as ZnIn<sub>2</sub>S<sub>4</sub>/Ti<sub>3</sub>C<sub>2</sub>T<sub>x</sub>, S-vacancies modified ZnIn<sub>2</sub>S<sub>4-x</sub>/Ti<sub>3</sub>C<sub>2</sub>, and Ti<sub>3</sub>C<sub>2</sub>/ZnIn<sub>2</sub>S<sub>4</sub>, accelerates the transfer and separation of photogenerated electrons from ZnIn<sub>2</sub>S<sub>4</sub> [16–18]. Our previous report also demonstrated that the interface interaction between ZnIn<sub>2</sub>S<sub>4</sub> and Mo<sub>2</sub>TiC<sub>2</sub> MXene establishes a pathway for the directional transfer of photogenerated electrons to Mo<sub>2</sub>TiC<sub>2</sub> [19]. However, the investigation of MXene-Ru as a co-catalyst of ZnIn<sub>2</sub>S<sub>4</sub> to manipulate the storage-release behavior of photogenerated electrons to synergistically improve electron utilization efficiency has not been reported.

Herein, a ZnIn<sub>2</sub>S<sub>4</sub>/Mo<sub>2</sub>TiC<sub>2</sub>-Ru composite was designed by coupling ZnIn<sub>2</sub>S<sub>4</sub> photocatalyst on the Mo<sub>2</sub>TiC<sub>2</sub>-Ru capacitance cocatalysts, enabling PHE reaction through alternating light-dark conditions. X-ray photoemission spectroscopy (XPS), charge density difference, in-situ Kelvin probe force microscopy (in-situ KPFM), dark-light Mott-Schottky and capacitance tests confirmed that the electron transfer channel at the interface promotes the directional transfer and storage of photogenerated electrons to Mo<sub>2</sub>TiC<sub>2</sub>-Ru, and then improves the separation efficiency of photogenerated charge. Linear sweep voltammetry (LSV) test and DFT calculation showed that the strong interaction and electron-rich environment of Mo<sub>2</sub>TiC<sub>2</sub>-Ru synergistically promotes surface water dissociation and hydrogen release kinetics. Moreover, open-circuit voltage decay (OCVD), quasi in-situ UV-vis diffuse reflectance spectra (quasi in-situ DRS) and in-situ electron paramagnetic resonance EPR (in-situ EPR) proved that the photogenerated electrons stored by

Mo<sub>2</sub>TiC<sub>2</sub>-Ru can be further released under dark conditions, so that the catalyst can continue to maintain a certain PHE activity. Therefore, ZnIn<sub>2</sub>S<sub>4</sub>/Mo<sub>2</sub>TiC<sub>2</sub>-Ru not only exhibits significantly increased PHE activity of 5.72 mmol·g<sup>-1</sup>·h<sup>-1</sup> under visible light, which is 5.78 and 1.94 times higher than that of ZnIn<sub>2</sub>S<sub>4</sub> and ZnIn<sub>2</sub>S<sub>4</sub>/Mo<sub>2</sub>TiC<sub>2</sub>, respectively, but also exhibits an HER rate of ~1.67 mmol·g<sup>-1</sup>·h<sup>-1</sup> under dark conditions. This study provides reference and guidance for the development of capacitive cocatalysts with an “electron-parking” engineering for efficient and sustained PHE reactions.

## 2. Experimental

### 2.1. Synthesis of Mo<sub>2</sub>TiC<sub>2</sub> MXene nanosheets

Mo<sub>2</sub>TiC<sub>2</sub> nanosheets were prepared by exfoliating the Al layers from Mo<sub>2</sub>TiAlC<sub>2</sub> as reported previously[19]. First, 1.0 g of Mo<sub>2</sub>TiAlC<sub>2</sub> powders was slowly added to 40 mL HF solution (49%) and continuously stirred at 55 °C for 48 h to remove the Al layers. The etched solid was repeatedly washed and centrifuged with H<sub>2</sub>O until the pH of the supernatant reached ~6, and then freeze-dried to remove the water in the samples. Second, the freeze-dried samples were added to 10 mL TBAOH and continuously stirred for 24 h for intercalation. Subsequently, the solids were separated by centrifugation and added to 50 mL H<sub>2</sub>O by ultrasound for 1 h for delamination. The suspension was centrifuged at 3500 r.p.m. for 1 h and the supernatant was collected, which was the colloidal solution of Mo<sub>2</sub>TiC<sub>2</sub> nanosheets, the concentration was determined as 2 mg/mL by freeze-drying.

### 2.2. Synthesis of Mo<sub>2</sub>TiC<sub>2</sub>-Ru

10 mL of 2 mg/mL Mo<sub>2</sub>TiC<sub>2</sub> solution was mixed with H<sub>2</sub>O to 20 mL and stirred continuously in Ar atmosphere. The RuCl<sub>3</sub> solution (10 mg/mL) in different volumes (0.41, 1.23, 2.05, 2.87, 4.10 mL) was added with H<sub>2</sub>O to 40 mL respectively, and then slowly dripped to the above Mo<sub>2</sub>TiC<sub>2</sub> solution (the flow rate was controlled by a peristaltic pump at 0.5 mL/min). After stirring for 1 h, 10 mL 0.5 mol/L NaBH<sub>4</sub> solution was slowly dripped into the above solution and continuously stirred for 24 h. Then the resulting suspension was repeatedly washed and centrifuged with H<sub>2</sub>O, and finally freeze-dried to obtain Mo<sub>2</sub>TiC<sub>2</sub>-Ru, labeled as MR-x (x=10, 30, 50, 70, 100, representing the weight ratio (wt%) of Ru to Mo<sub>2</sub>TiC<sub>2</sub>).

### 2.3. Synthesis of ZnIn<sub>2</sub>S<sub>4</sub>/Mo<sub>2</sub>TiC<sub>2</sub>-Ru

According to our previous report, the mass ratio of Mo<sub>2</sub>TiC<sub>2</sub> to ZnIn<sub>2</sub>S<sub>4</sub> was 1.56 wt% in ZnIn<sub>2</sub>S<sub>4</sub>/Mo<sub>2</sub>TiC<sub>2</sub> [19]. 6.6 mg (1.56 wt%) of the above MR-X (X=10, 30, 50, 70, 100) powders were respectively dispersed in 60 mL of H<sub>2</sub>O with ultrasound in a Ar atmosphere for 1 h and the pH was adjusted to 3 by HCl. ZnCl<sub>2</sub> (1 mmol), InCl<sub>3</sub> (2 mmol), and TAA (8 mmol) were added to the above solution. After stirring for 30 min, the homogeneous suspension was transferred into a 100 mL Teflon-lined autoclave and maintained at 180 °C for 24 h. After cooling, the products were collected by washed and filtered with H<sub>2</sub>O and ethanol for several times, and vacuum-dried overnight at 60 °C. The composites were labeled as ZMR-x (x=0.16, 0.47, 0.78, 1.09 and 1.56, representing the weight ratio wt% of Ru to ZnIn<sub>2</sub>S<sub>4</sub>). The actual contents of Ru relative to ZnIn<sub>2</sub>S<sub>4</sub> in ZMR-0.16, ZMR-0.47, ZMR-0.78, ZMR-1.09 and ZMR-1.56 were determined by inductively coupled plasma optical emission spectroscopy (ICP-OES) as 0.13, 0.35, 0.62, 0.91, 1.32 wt% respectively. For comparison purposes, pristine ZnIn<sub>2</sub>S<sub>4</sub> (labeled as ZIS) and ZnIn<sub>2</sub>S<sub>4</sub>/Mo<sub>2</sub>TiC<sub>2</sub> (labeled as ZM) were prepared under the same conditions, except that the former did not add Mo<sub>2</sub>TiC<sub>2</sub>-Ru, and the latter replaced Mo<sub>2</sub>TiC<sub>2</sub>-Ru with Mo<sub>2</sub>TiC<sub>2</sub>.

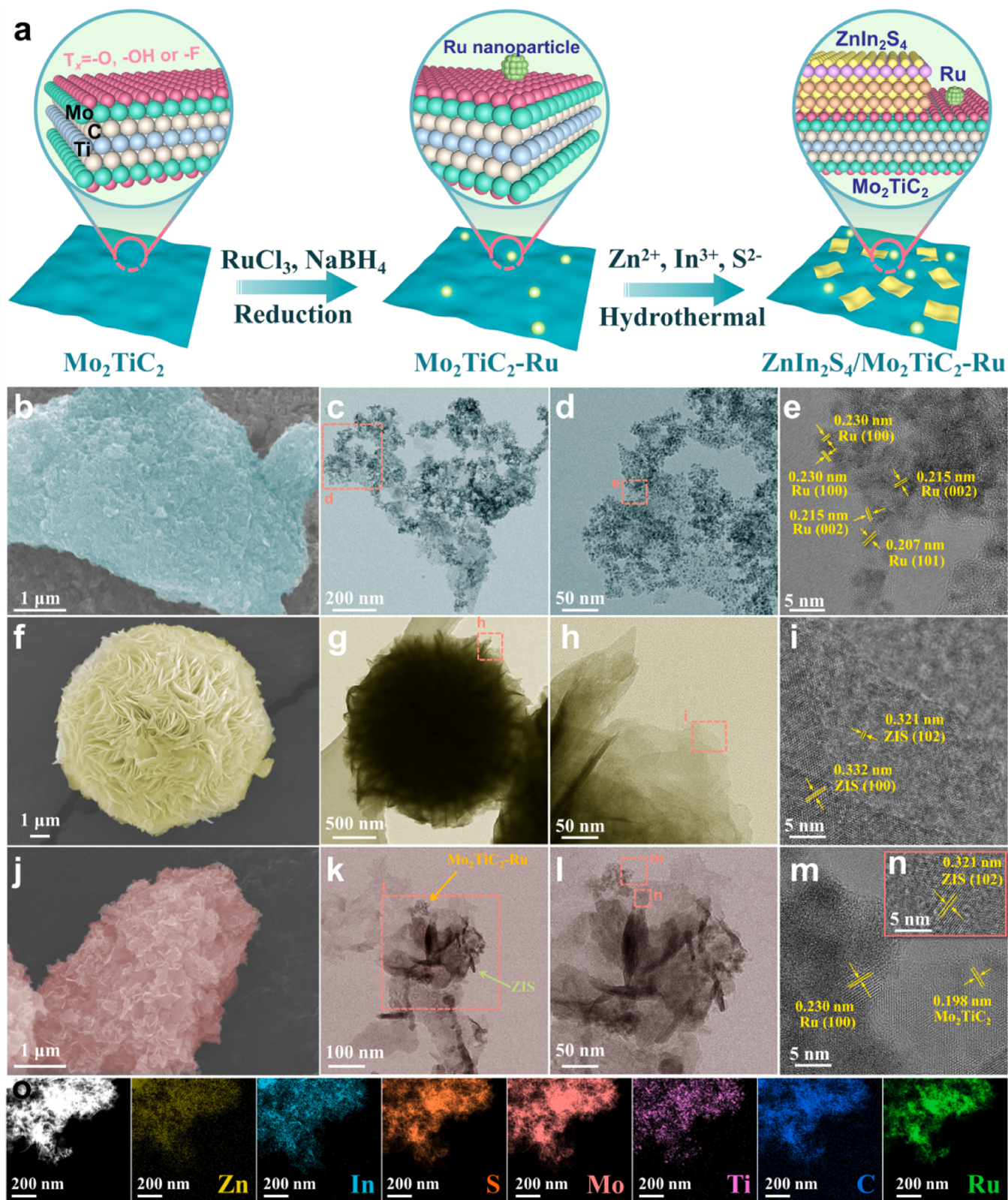


**Fig. 1.** (a) Schematic illustration for the synthetic procedure of ZnIn<sub>2</sub>S<sub>4</sub>/Mo<sub>2</sub>TiC<sub>2</sub>-Ru photocatalyst. SEM (b) and TEM (c-e) images of MR-50. SEM (f) and TEM (g-i) images of ZIS. SEM (j) and TEM (k-n) images of ZMR-0.78. (o) TEM image and corresponding element (Zn, In, S, Mo, Ti, C, and Ru) mappings of ZMR-0.78.

### 3. Results and discussion

#### 3.1. Synthesis and characterizations of ZnIn<sub>2</sub>S<sub>4</sub>/Mo<sub>2</sub>TiC<sub>2</sub>-Ru

ZnIn<sub>2</sub>S<sub>4</sub>/Mo<sub>2</sub>TiC<sub>2</sub>-Ru composites were synthesized by room-temperature NaBH<sub>4</sub> reduction combined with hydrothermal methods, as illustrated in Fig. 1a. Firstly, RuCl<sub>3</sub> solution was slowly added to Mo<sub>2</sub>TiC<sub>2</sub> solution, and NaBH<sub>4</sub> was used as the reducing agent to reduce adsorbed Ru<sup>3+</sup> on Mo<sub>2</sub>TiC<sub>2</sub> to Ru<sup>0</sup> in the metallic state, resulting in the formation of Mo<sub>2</sub>TiC<sub>2</sub>-Ru. Subsequently, as the electrostatic adsorption of Mo<sub>2</sub>TiC<sub>2</sub> with Zn<sup>2+</sup>/In<sup>3+</sup> cations, ZnIn<sub>2</sub>S<sub>4</sub> was synthesized in situ on

Mo<sub>2</sub>TiC<sub>2</sub>-Ru by hydrothermal method [19].

The morphology and structure of ZnIn<sub>2</sub>S<sub>4</sub>/Mo<sub>2</sub>TiC<sub>2</sub>-Ru were observed using scanning electron microscopy (SEM) and transmission electron microscopy (TEM), as shown in Fig. 1. Figs. S1–3 depict the successful synthesis of Mo<sub>2</sub>TiC<sub>2</sub> nanosheets, with a lattice spacing of 0.198 nm. Fig. 1b shows that the MR-50 surface becomes notably rough, which is attributed to the substantial loading of Ru NPs on the Mo<sub>2</sub>TiC<sub>2</sub> (Fig. 1c–e). The lattice spacings 0.230, 0.215, and 0.207 nm correspond to the (100), (002) and (101) crystal planes of Ru NPs, respectively [20]. Fig. 1f–h show that ZIS forms microscale flower-shaped aggregates composed of stacked nanosheets. The lattice spacings 0.321 nm and

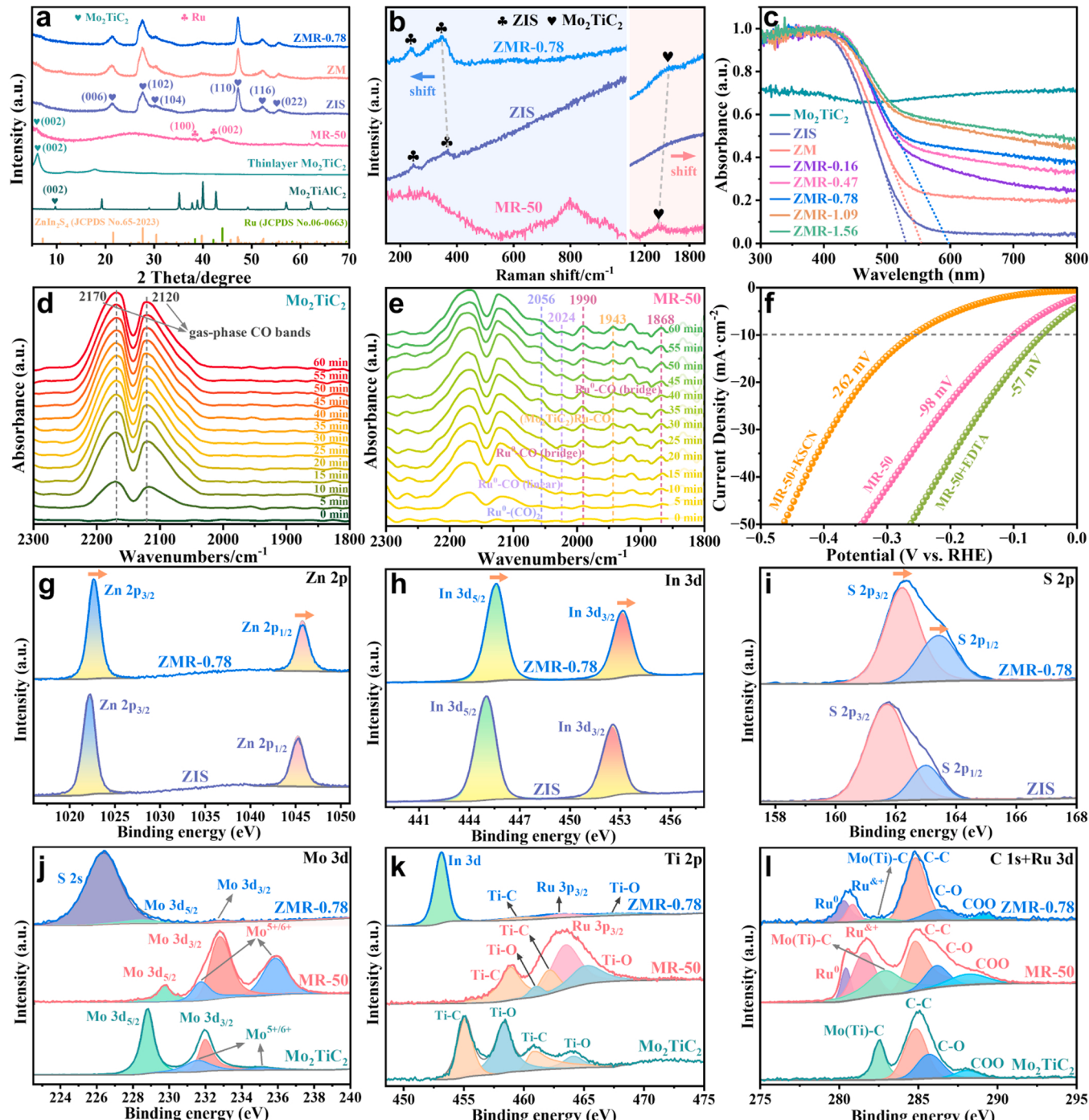


**Fig. 2.** (a) XRD patterns of as-prepared samples. (b) Raman spectra of MR-50, ZIS, and ZMR-0.78. (c) DRS spectra of as-prepared samples. In-situ DRIFTS spectra of (d) Mo<sub>2</sub>TiC<sub>2</sub> and (e) MR-50 under 10 vol% CO/Ar gas flowing. (f) Catalyst poisoning experiment for MR-50 in 1 M KOH with the addition of 5 mM KSCN or 5 mM of EDTA. (g–l) XPS spectrum of Zn 2p (g), In 3d (h), S 2p (i), Mo 3d (j), Ti 2p (k), C 1 s and Ru 3d (l) for ZIS, Mo<sub>2</sub>TiC<sub>2</sub>, MR-50, and ZMR-0.78.

0.332 nm (**Fig. 1i**) correspond to the (102) and (100) crystal planes of ZIS, respectively [21]. In **Fig. 1j-l**, a large number of small-size ZIS nanosheets were observed on the large-size Mo<sub>2</sub>TiC<sub>2</sub>-Ru in ZMR-0.78, and **Fig. 1m-n** exhibits the coexistence and interfacial contact of ZIS, Mo<sub>2</sub>TiC<sub>2</sub>, and Ru. In addition, TEM mapping in **Fig. 1o** and SEM mapping in **Fig. S4** observed the coexistence and uniform dispersion of elements Zn, In, S, Mo, Ti, C, and Ru, further confirming the successful synthesis of the ZnIn<sub>2</sub>S<sub>4</sub>/Mo<sub>2</sub>TiC<sub>2</sub>-Ru composite.

The phase composition and existence form of ZnIn<sub>2</sub>S<sub>4</sub>/Mo<sub>2</sub>TiC<sub>2</sub>-Ru were further explored, as shown in **Fig. 2**. The phase structure of the as-prepared samples was determined through X-ray diffraction (XRD) characterization, as shown in **Fig. 2a**. Compared to Mo<sub>2</sub>TiAlC<sub>2</sub>, the (002) peak of Mo<sub>2</sub>TiC<sub>2</sub> shifted to about 6° with an increased intensity, while the characteristic peak of Mo<sub>2</sub>TiAlC<sub>2</sub> disappeared, indicating the successful synthesis of Mo<sub>2</sub>TiC<sub>2</sub> nanosheets [22]. The loading of Ru is confirmed by the characteristic peaks corresponding to the hexagonal Ru (JCPDS No. 06-0663) on (100) and (002) in MR-50 [23]. The ZIS sample exhibits excellent compatibility with the hexagonal ZnIn<sub>2</sub>S<sub>4</sub> (JCPDS No. 65-2023) [24]. Mo<sub>2</sub>TiC<sub>2</sub>-Ru did not alter the phase structure of ZIS (**Fig. S5**), and their peaks were not clearly observed due to the low content and homogeneous dispersion [25]. The Raman spectra in **Fig. S6** confirms the strong interface interaction between Ru NPs and Mo<sub>2</sub>TiC<sub>2</sub>. In **Fig. 2b**, ZIS and MR-50 simultaneously appear in the Raman spectrum of ZMR-0.78, implying their coexistence in the composite. Furthermore, the characteristic peaks of ZIS and MR-50 exhibit shifts towards shorter and longer wavelengths respectively, indicating a strong interaction [26]. The UV-vis diffuse reflectance spectra (DRS) in **Fig. 2c** exhibits the outstanding visible light responsive capability of ZIS, with an absorption edge near 532 nm. Black Mo<sub>2</sub>TiC<sub>2</sub> exhibits excellent absorption ability across the entire spectrum, thereby enhancing the light absorption and response capability [27]. With the increasing Ru content, the light absorption and responsiveness of ZMR gradually improve. **Fig. S7-9** illustrates that the bandgap value of ZIS is 2.51 eV, with valence band E<sub>VB</sub> and conduction band E<sub>CB</sub> at 1.07 and -1.44 V vs. NHE, pH=7, respectively. The detailed band structure diagram of ZnIn<sub>2</sub>S<sub>4</sub>/Mo<sub>2</sub>TiC<sub>2</sub>-Ru is shown in **Fig. S10**.

The Ru species loaded on Mo<sub>2</sub>TiC<sub>2</sub> and their interaction were characterized by in situ diffuse reflectance infrared fourier transform spectroscopy (in situ DRIFTS) using CO as a probe. Gas-phase CO bands from persistent CO flow were detected at 2120 and 2170 cm<sup>-1</sup> in both Mo<sub>2</sub>TiC<sub>2</sub> and MR-50 [28]. Mo<sub>2</sub>TiC<sub>2</sub> in **Fig. 2d** shows no additional CO adsorption band. In contrast, MR-50 in **Fig. 2e** shows different CO absorption bands in the 1868–2056 cm<sup>-1</sup>. The peak at 2056 cm<sup>-1</sup> is assigned to dicarbonyl CO species adsorbed on metallic Ru (Ru<sup>0</sup>) in the formed of Ru<sup>0</sup>-(CO)<sub>2</sub> [29,30]. The peak at 2024 cm<sup>-1</sup> is attributed to the linear adsorption CO on Ru<sup>0</sup> [30]. The peaks at 1990 and 1868 cm<sup>-1</sup> belong to CO bridge adsorption on Ru NPs [31,32]. The above CO adsorption forms verify the reduction of Ru NPs on Mo<sub>2</sub>TiC<sub>2</sub>. In addition, the peak at 1943 cm<sup>-1</sup> is attributed to CO adsorption on metal sites strongly interacting with the support in the formed of (Mo<sub>2</sub>TiC<sub>2</sub>)Ru-CO [32]. The Ru species were further identified using potassium thiocyanate (KSCN) and ethylenediaminetetraacetic acid (EDTA) as poisoning species. The SCN<sup>-</sup> is readily adsorbed onto the Ru NPs, while EDTA primarily forms coordination bonds with Ru single atoms or nano-clusters to block the sites [33]. From **Fig. 2f**, the η<sub>10</sub> value of MR-50 (-98 mV) exhibited a slight shift to -57 mV upon the addition of EDTA, while it underwent a significant shift to -262 mV upon the addition of KSCN. For comparison, the η<sub>10</sub> value of Mo<sub>2</sub>TiC<sub>2</sub> in **Fig. S11** did not show significant changes after the addition of EDTA and KSCN. The above poisoning test confirmed the loading of Ru NPs on the Mo<sub>2</sub>TiC<sub>2</sub>.

The chemical composition and electronic state of the material surface were determined through XPS, as shown in **Fig. 2g-l**. The survey spectrum is shown in **Fig. S12**. **Fig. 2g-i** display the high-resolution spectra of Zn 2p, In 3d, and S 2p for ZIS [34]. In comparison to ZIS, Zn 2p, In 3d, and S 2p in ZMR-0.78 have all shifted towards higher

binding energies, indicating a decrease in surface electron density and surface electrons loss from ZIS [35]. **Fig. 2j-k** show the high-resolution spectra of Mo 3d and Ti 2p for Mo<sub>2</sub>TiC<sub>2</sub> [22]. The spectra of Mo 3d and Ti 2p in ZMR-0.78 have undergone notable changes due to the interference S 2s and In 3d of ZIS [36]. Compared to MR-50, ZMR-0.78 exhibits a decrease in binding energies for both Mo 3d and Ti 2p, which suggests an increase in surface electronic density of Mo<sub>2</sub>TiC<sub>2</sub>-Ru [37]. The binding energy shift confirms the electrons transfer from ZIS to Mo<sub>2</sub>TiC<sub>2</sub>-Ru. **Fig. 2l** and **Fig. S13** show the high-resolution spectra of Ru 3d and Ru 3p respectively [20]. The appearance of Ru<sup>0</sup>, Ru<sup>&+</sup> and Ru 3p<sub>3/2</sub> in ZMR-0.78 demonstrates the existence of Ru NPs [38]. In addition, the F 1 s in **Fig. S14** of Mo<sub>2</sub>TiC<sub>2</sub>-Ru and ZMR-0.78 disappeared compared to Mo<sub>2</sub>TiC<sub>2</sub>. This indicates that during the reduction of Ru NPs and the hydrothermal process, the -F terminal groups on the surface of Mo<sub>2</sub>TiC<sub>2</sub> were transformed to -O, which is beneficial for the reaction of PHE [16]. The above XPS analysis confirmed the successful preparation of ZnIn<sub>2</sub>S<sub>4</sub>/Mo<sub>2</sub>TiC<sub>2</sub>-Ru photocatalyst and revealed the establishment of an electron transfer pathway from ZIS to Mo<sub>2</sub>TiC<sub>2</sub>-Ru, facilitating electron storage in Mo<sub>2</sub>TiC<sub>2</sub>-Ru “electron-parking”.

### 3.2. The formation of electron-rich environment

The transfer of photogenerated electrons and the formation of electron-rich environment in ZnIn<sub>2</sub>S<sub>4</sub>/Mo<sub>2</sub>TiC<sub>2</sub>-Ru were investigated. In **Fig. 3a**, the electron loss (blue part) of ZIS and electron enrichment (yellow part) of Mo<sub>2</sub>TiC<sub>2</sub> at the interface indicate the regulation of electron structure and a trend of electron transfer from ZIS to Mo<sub>2</sub>TiC<sub>2</sub> [16]. Moreover, the electron distribution at the Mo<sub>2</sub>TiC<sub>2</sub>-Ru interface shows a depletion of Ru and an enrichment of electrons at Mo<sub>2</sub>TiC<sub>2</sub> interface in **Fig. 3b**, which attributed to the strong metal-support interaction with synergistic effects [39]. **Fig. 3c** presents the visual electron distribution among ZIS, Mo<sub>2</sub>TiC<sub>2</sub>, and Ru. The electron transfer behavior of the composite was further determined by the surface potential distribution using in-situ KPBM under dark-light conditions. The AFM images of ZM and ZMR-0.78 are shown in **Fig. S15**. The surface potential difference of ZM under illumination is ~261 mV (**Fig. 3e, g**), which is larger than the ~170 mV (**Fig. 3d, f**) observed in the dark, indicating the generation and separation of electron-holes under illumination [40]. Comparatively, ZMR-0.78 exhibits a more significant increase in surface potential difference under illumination, measuring ~546 mV (**Fig. 3i, k**) compared to ~341 mV (**Fig. 3h, j**) in the dark, indicating an enhanced separation of electron-hole pairs. Additionally, the decrease in surface potential of Mo<sub>2</sub>TiC<sub>2</sub>-Ru implies the accumulation of electrons and an increase in electron density, creating a favorable electron-rich environment in the “electron-parking” [40].

The charge transfer and separation mechanism of ZnIn<sub>2</sub>S<sub>4</sub>/Mo<sub>2</sub>TiC<sub>2</sub>-Ru was understood through the flat band potential (V<sub>fb</sub>) measured by Mott-Schottky analysis under dark-light conditions. Band bending at the photocatalyst/electrolyte interface attracts holes while pushing electrons away. Therefore, as the charge density increases under illumination, the V<sub>fb</sub> becomes more negative and the slope decreases, intensifying the band bending to maintain the Fermi level balance [41]. Due to the large number of photogenerated electron-hole recombination in the bulk phase, the V<sub>fb</sub> of ZIS is only slightly shifted after illumination (**Fig. 3l**) [42]. In contrast, the V<sub>fb</sub> of ZM (**Fig. 3m**) and ZMR-0.78 (**Fig. 3n**) showed obvious negative shift after illumination, and the shift amplitude of ZMR-0.78 was larger. This indicates that the electron-rich environment in the “electron-parking” is beneficial for inhibiting the backflow of electrons [43].

### 3.3. The role and function of electron-rich environment

The formation of the electron-rich environment has brought two beneficial improvements to the PHE reaction of ZnIn<sub>2</sub>S<sub>4</sub>/Mo<sub>2</sub>TiC<sub>2</sub>-Ru: (1) photoinduced charges separation; (2) photoinduced charges surface reaction kinetics. We first investigated the influence of electron-rich

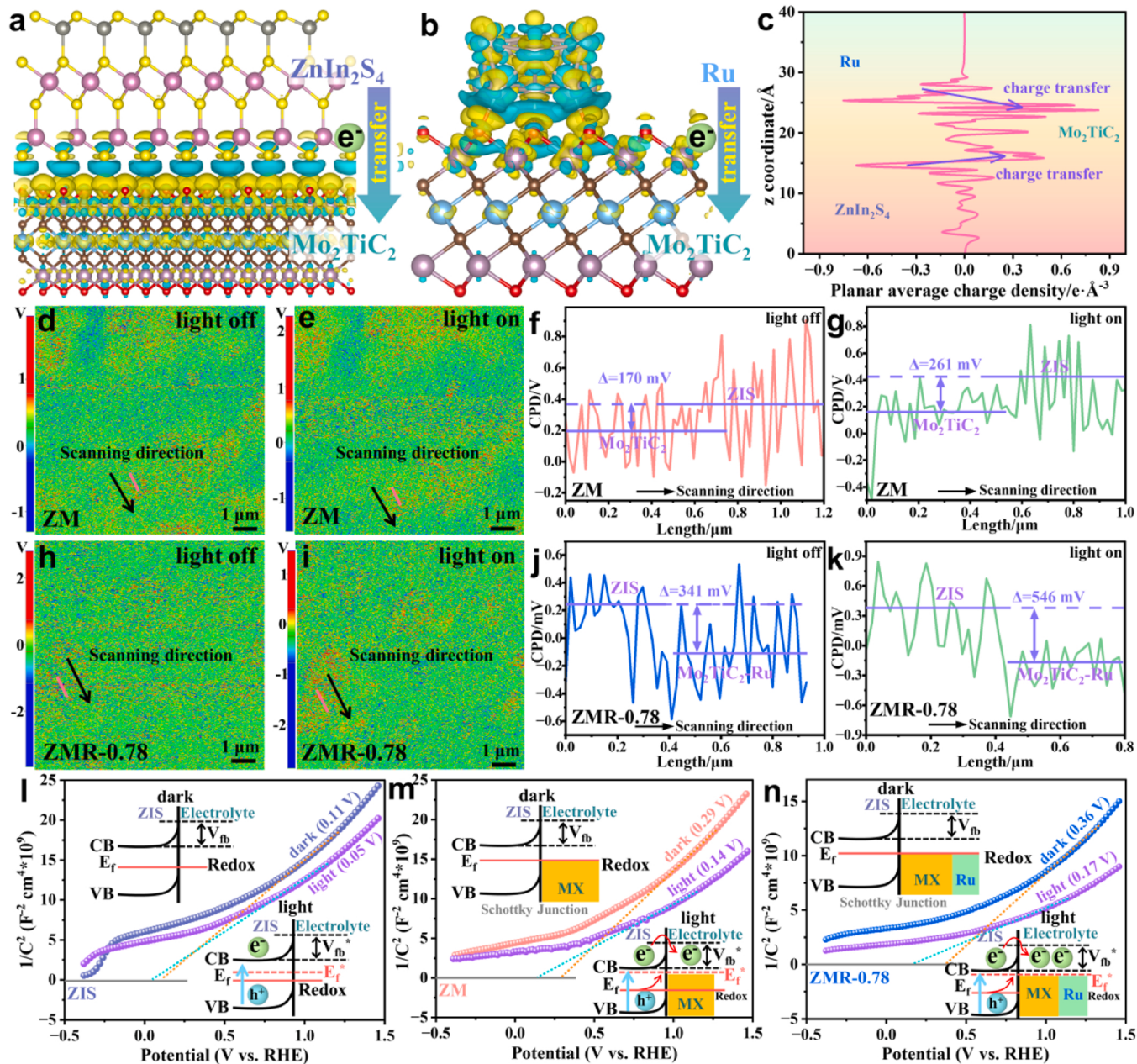


**Fig. 3.** The charge density difference of (a)  $\text{ZnIn}_2\text{S}_4/\text{Mo}_2\text{TiC}_2$  and (b)  $\text{Mo}_2\text{TiC}_2$ -Ru, where the yellow and blue regions correspond to high and low electron density, respectively. (c) The corresponding plane-averaged charge density plot along the vertical direction. KPFM images of ZM before (d) and after (e) irradiation. (f) the corresponding vertical distribution of surface potential in d. (g) the corresponding vertical distribution of surface potential in e. KPFM images of ZMR-0.78 before (h) and after (i) irradiation. (j) the corresponding vertical distribution of surface potential in h. (k) the corresponding vertical distribution of surface potential in i. Mott-Schottky plots of (l) ZIS, (m) ZM, and (n) ZMR-0.78 under dark and light conditions.

environment on the photogenerated electron-hole separation behavior. In Fig. S16, the photocurrent intensity of ZIS, ZM, and ZMR-0.78 under illumination shows an increasing trend, indicating an improvement in the separation efficiency of electrons and holes [44,45]. Fig. S17 shows that the charge separation efficiency of ZMR-0.78 (70.6%) is 1.75 and 1.06 times that of ZIS (40.3%) and ZM (66.4%), respectively [46]. The transient surface photovoltage (TPV) in Fig. S18 shows that the photogenerated electrons in ZMR-0.78 are diffused and transferred, which promotes the efficiency of photogenerated separation [47]. The semi-circle diameters of ZIS, ZM and ZMR-0.78 in impedance spectroscopy EIS (Fig. S19) decrease successively, representing the decrease of interfacial charge transfer resistance [48,49]. In Fig. S20, the steady-state photoluminescence (PL) intensity of ZIS, ZM, and ZMR-0.78

decreases gradually, indicating a gradual decrease in carrier recombination rate [50,51]. In time-resolved photoluminescence (TRPL) spectra (Fig. S21 and Table S1), the fluorescence lifetimes of ZIS (2.25 ns), ZM (1.50 ns) and ZMR-0.78 (1.27 ns) are gradually reduced, which is attributed to the presence of non-radiative decay pathways in the composite, confirming the existence of electron transport channels in  $\text{ZnIn}_2\text{S}_4/\text{Mo}_2\text{TiC}_2$ -Ru [52]. The above results indicate that the stored electrons from  $\text{ZnIn}_2\text{S}_4$  to  $\text{Mo}_2\text{TiC}_2$ -Ru “electron-parking” as a directional transfer improve the spatial separation efficiency of photogenerated electrons.

Another advantageous improvement resulting from the electron-rich environment is the optimization of surface reaction kinetics, for which we investigated the HER reaction behavior involving water dissociation

( $\text{H}^* + \text{H}_2\text{O} + \text{e}^- \rightarrow \text{H}_2 + \text{OH}^-$ ) and hydrogen release ( $\text{H}^* + \text{H}^* \rightarrow \text{H}_2 + 2\text{H}^*$ ) processes on surface of  $\text{Mo}_2\text{TiC}_2$ -Ru as the photogenerated electron acceptor. The calculated water dissociation energy ( $\Delta G_{\text{H}_2\text{O-dis}}$ ) of  $\text{Mo}_2\text{TiC}_2$ , Ru NPs, and  $\text{Mo}_2\text{TiC}_2$ -Ru are shown in Fig. 4a.  $\text{Mo}_2\text{TiC}_2$  exhibits poor  $\Delta G_{\text{H}_2\text{O-dis}}$  (2.81 eV), which impedes the generation of  $\text{H}^*$ , while Ru NPs possess strong  $\Delta G_{\text{H}_2\text{O-dis}}$  ( $-0.85$  eV). The modification of  $\text{Mo}_2\text{TiC}_2$  by Ru NPs enhances the adsorption ( $-0.827$  eV) and dissociation ( $-0.834$  eV) of water. Fig. 4b shows the calculated hydrogen adsorption energies ( $\Delta G_{\text{H}^*}$ ) of  $\text{Mo}_2\text{TiC}_2$ , Ru NPs, and  $\text{Mo}_2\text{TiC}_2$ -Ru. The closer the  $\Delta G_{\text{H}^*}$  is to zero, the more favorable it is for the adsorption/desorption equilibrium of  $\text{H}^*$  [53].  $\text{Mo}_2\text{TiC}_2$  exhibits a more favorable  $\Delta G_{\text{H}^*}$  ( $-0.35$  eV) compared to Ru NPs ( $-0.43$  eV), and the  $\Delta G_{\text{H}^*}$  of  $\text{Mo}_2\text{TiC}_2$ -Ru ( $0.06$  eV) is further improved. The d-band center theory provides a good description of the reasons for the variation in  $\Delta G_{\text{H}^*}$  [54]. The d-band centers of  $\text{Mo}_2\text{TiC}_2$ , Ru NPs, and  $\text{Mo}_2\text{TiC}_2$ -Ru were calculated using density of states (DOS) in Fig. S22. Fig. 4c shows a linear correlation between the  $\Delta G_{\text{H}^*}$  and the downward shift of the d-band center of Ru,  $\text{Mo}_2\text{TiC}_2$ , and  $\text{Mo}_2\text{TiC}_2$ -Ru. The downward shift of the d-band center indicates that the strong interaction between Ru and  $\text{Mo}_2\text{TiC}_2$  results in the filling of more anti-bonding orbitals by electrons, leading to an increase in Pauli repulsion and a decrease in bond strength [54]. The water dissociation ability of  $\text{Mo}_2\text{TiC}_2$ -Ru was investigated by electrochemical HER performance in 1.0 M KOH, as the sluggish water dissociation kinetics is the rate-determining step for alkaline HER [55]. The LSV curves in Fig. 4d show that MR-50 exhibits a significantly lower overpotential (103 mV vs. RHE) than  $\text{Mo}_2\text{TiC}_2$  (398 mV vs. RHE) at a current density of  $10 \text{ mA cm}^{-2}$ . The Tafel slope in Fig. 4e intuitively

compares the kinetic mechanism of  $\text{Mo}_2\text{TiC}_2$  and MR-50. The Tafel slope of  $\text{Mo}_2\text{TiC}_2$  ( $309 \text{ mV dec}^{-1}$ ) is much higher than  $120 \text{ mV dec}^{-1}$ , indicating that the sluggish water dissociation process limits the kinetic rate of the overall reaction [56]. Comparatively, the Tafel slope of MR-50 ( $80 \text{ mV dec}^{-1}$ ) is in the range of  $40$ – $120 \text{ mV dec}^{-1}$ , which means faster kinetics and the removal of water dissociation barrier, indicating that Volmer-Heyrovsky mechanism dominates the HER process [56]. The PHE activity of ZMR-0.78 in pure  $\text{H}_2\text{O}$  (without TEOA) was investigated, as shown in Fig. S23 and Fig. 4f. Both ZIS and ZM exhibited relatively low PHE rates, with  $1.18 \mu\text{mol g}^{-1} \cdot \text{h}^{-1}$  and  $8.70 \mu\text{mol g}^{-1} \cdot \text{h}^{-1}$ , respectively. However, the PHE rate of ZMR-0.78 reached  $69.7 \mu\text{mol g}^{-1} \cdot \text{h}^{-1}$ , which was 59.1 and 8.7 times higher than that of ZIS and ZM, respectively. The scarcity of  $\text{H}^+$  in the  $\text{H}_2\text{O}$  environment makes water dissociation process as the proton source for the HER process [57]. The improved performance of PHE in pure  $\text{H}_2\text{O}$  by ZMR-0.78 further validates that the electron-rich environment of  $\text{Mo}_2\text{TiC}_2$ -Ru accelerates the water dissociation kinetics.

Fig. 4g represents the synergistic enhancement of the reaction behavior on the  $\text{Mo}_2\text{TiC}_2$ -Ru surface using the metaphorical representation of a “eight diagrams”.  $\text{Mo}_2\text{TiC}_2$  has suitable hydrogen adsorption ability as active sites for HER, but exhibits poor water splitting capability. The Ru NPs possess strong water splitting capability, but exhibit excessive hydrogen adsorption. Integrated with the advantages of  $\text{Mo}_2\text{TiC}_2$  and Ru,  $\text{Mo}_2\text{TiC}_2$ -Ru achieves a simultaneous enhancement and balance of hydrogen adsorption energy and water dissociation energy, enabling rapid dissociation of  $\text{H}_2\text{O}$  on its surface and synergistic enhancement of  $\text{H}_2$  desorption. The above results show that the

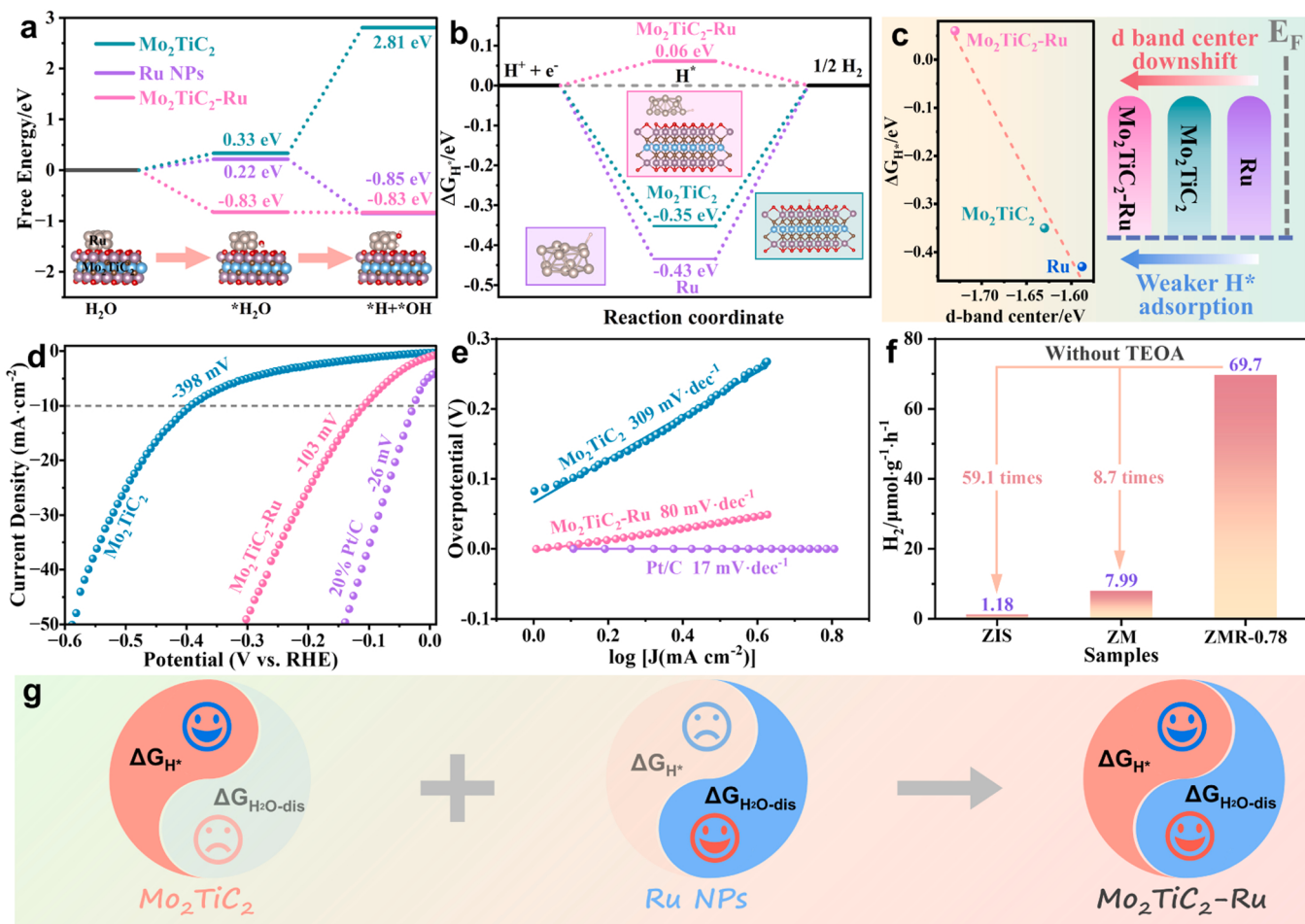


**Fig. 4.** (a) The water dissociation energy ( $\Delta G_{\text{H}_2\text{O-dis}}$ ) and (b) the Gibbs free energy ( $\Delta G_{\text{H}^*}$ ) of  $\text{Mo}_2\text{TiC}_2$ , Ru, and  $\text{Mo}_2\text{TiC}_2$ -Ru. (c) Correlation between  $\Delta G_{\text{H}^*}$  and d-band center, and schematic illustrating that the d-band. (d) Polarization curves, (e) Tafel plots of  $\text{Mo}_2\text{TiC}_2$  and  $\text{Mo}_2\text{TiC}_2$ -Ru. (f) The PHE rate of ZIS, ZM, and ZMR-0.78 (100 mg) in pure water (without TEOA). (g) Illustration of the improvement of  $\Delta G_{\text{H}_2\text{O-dis}}$  and  $\Delta G_{\text{H}^*}$  by  $\text{Mo}_2\text{TiC}_2$ -Ru.

electronic structure regulation of  $\text{Mo}_2\text{TiC}_2\text{-Ru}$  in electron-rich environment synergistically achieved the double improvement of water dissociation and hydrogen adsorption kinetics, which is conducive to promoting the rapid reaction of enriched electrons and improving the PHE efficiency.

### 3.4. Photocatalytic hydrogen evolution activity of $\text{ZnIn}_2\text{S}_4/\text{Mo}_2\text{TiC}_2\text{-Ru}$

The advantage of improved carrier separation efficiency and accelerated reaction kinetics from the electron-rich environment of  $\text{Mo}_2\text{TiC}_2\text{-Ru}$  determines the PHE performance. A comprehensive investigation was conducted to extensively examine the PHE activity of  $\text{ZnIn}_2\text{S}_4/\text{Mo}_2\text{TiC}_2\text{-Ru}$  under visible light irradiation ( $>420 \text{ nm}$ ), using TEOA as a hole sacrificial agent. The hydrogen production does not exhibit a linear increase with the amount of photocatalyst [58]. Consequently, the PHE activity of ZMR-0.78 was investigated at various dosages. Fig. S24

illustrates that ZM-0.78 exhibited the optimum PHE rate of  $r_{\text{opt}}=572 \mu\text{mol}\cdot\text{h}^{-1}$  at 100 mg. The PHE test of the ZMR series photocatalyst is shown in Fig. 5a, and all photocatalysts showed a good linear increase in hydrogen production within 4 h.  $\text{Mo}_2\text{TiC}_2\text{-Ru}$  cocatalyst has no hydrogen evolution activity under visible light irradiation, eliminating the possibility of its photothermal decomposition of TEOA and  $\text{H}_2\text{O}$  to produce hydrogen. Fig. 5b illustrates a “volcano-like” trend in the PHE rate of the ZMR catalyst, with an initial increase followed by a subsequent decrease as the Ru content increases. At a relative content of 0.78 wt% Ru compared to ZIS, ZMR-0.78 exhibits the highest PHE rate of  $5.72 \text{ mmol}\cdot\text{g}^{-1}\cdot\text{h}^{-1}$ , which are 5.78 and 1.94 times higher than that of ZIS ( $0.99 \text{ mmol}\cdot\text{g}^{-1}\cdot\text{h}^{-1}$ ) and ZM ( $2.95 \text{ mmol}\cdot\text{g}^{-1}\cdot\text{h}^{-1}$ ), respectively. The uniqueness of the high PHE activity of ZMR-0.78 was verified through different Ru introduction methods. As shown in Fig. S25, the PHE rates of ZMR-0.78 are 2.79 and 1.51 times higher than ZIS+0.78 wt %Ru ( $2.05 \text{ mmol}\cdot\text{g}^{-1}\cdot\text{h}^{-1}$ ) and ZM+0.78 wt%Ru ( $3.78 \text{ mmol}\cdot\text{g}^{-1}\cdot\text{h}^{-1}$ ),

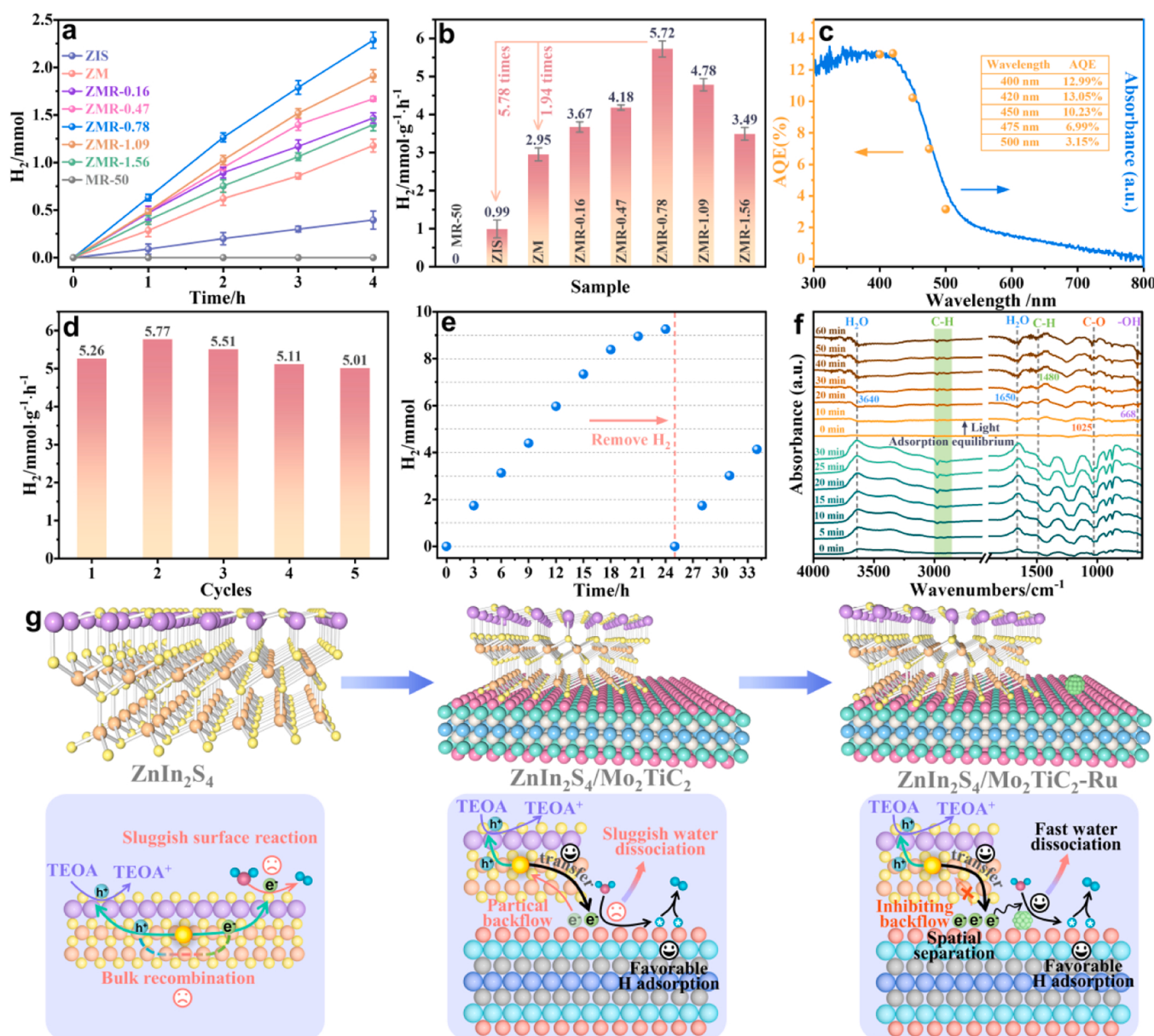


**Fig. 5.** (a) Time-dependent PHE activity and (b)PHE rate of different photocatalysts under visible light irradiation ( $\lambda>420 \text{ nm}$ ). The experiments were repeated three times in parallel to calculate the average values and error bars. (c) AQE of ZMR-0.78 at different single wavelengths. (d) The cycle stability test and (e) continuous PHE experimental curve of ZMR-0.78 in 100 mL of 10 vol% TEOA solution. (f) In situ DRIFTS spectroscopy of the reaction behavior of  $\text{H}_2\text{O}$  and TEOA on ZMR-0.78 during the simulated PHE process. (g) Schematic of the mechanism for promoting PHE process by  $\text{ZnIn}_2\text{S}_4/\text{Mo}_2\text{TiC}_2\text{-Ru}$ .

respectively, indicating that the improvement in PHE performance is a result of the synergistic effect among the components of  $\text{ZnIn}_2\text{S}_4/\text{Mo}_2\text{TiC}_2\text{-Ru}$ . Similarly, the AQE value of the photocatalyst does not increase linearly with the increase in catalyst dosage [58]. Therefore, the AQE value of ZMR-0.78 at 420 nm was investigated for different catalyst dosages in Fig. S26. The optimal AQE value of ZMR-0.78 is  $\text{AQE}_{\text{opt}}=13.05\%$  at 100 mg. Moreover, the PHE activity and rate of ZMR-0.78 were tested at different single wavelengths in Fig. S27. Fig. 5c shows that the AQE values of ZMR-0.78 at different wavelengths (400, 420, 450, 475, and 500 nm) are in good agreement with its optical response spectra.

Fig. 5d and Fig. S28 show that the PHE rate of ZM-0.78 remained stable throughout the 5-cycle experiments. The hydrogen production of ZMR-0.78 exhibits a sustained linear increase over a 24 h period as depicted in Fig. 5e. Although  $\text{H}_2$  increases slowly between 18 and 24 h, the PHE rate restores to its initial state under continued illumination after  $\text{H}_2$  is removed from the system. The decrease in rate may be attributed to the saturation of  $\text{H}_2$  in the system rather than catalyst deactivation or excessive consumption of TEOA. Cycle experiments and sustainable testing have conclusively demonstrated the excellent cycling stability and sustainable application capabilities of ZMR-0.78. The XRD patterns in Fig. S29 and SEM images in Fig. S30 show that there is no significant change in the phase structure and morphology of ZMR-0.78 after the reaction, confirming the excellent structural stability of  $\text{ZnIn}_2\text{S}_4/\text{Mo}_2\text{TiC}_2\text{-Ru}$  in the PHE reaction. The reaction behavior of  $\text{H}_2\text{O}$  and TEOA during the PHE process on ZMR-0.78 was investigated by in situ infrared spectroscopy, as shown in Fig. 5f. Under dark conditions, various spectral features were observed during the adsorption process. Specifically, the bending mode of water at  $1650\text{ cm}^{-1}$  and the characteristic peak of water at  $3640\text{ cm}^{-1}$  gradually emerged [8]. Additionally, the stretching vibration of C-H near  $2850\text{--}3000\text{ cm}^{-1}$ , and the stretching vibration of the alcohol hydroxyl group at  $668\text{ cm}^{-1}$  were also detected [59]. These observations provide clear evidence of the adsorption of  $\text{H}_2\text{O}$  and TEOA on ZMR-0.78, which reaches equilibrium after 30 minutes. Under light irradiation, the characteristic peaks associated with  $\text{H}_2\text{O}$  and TEOA gradually disappear, while the stretching vibration of C-O at  $1025\text{ cm}^{-1}$  gradually emerges. This gradual emergence may be attributed to the oxidation of alcohol hydroxyl groups, indicating the collective involvement of  $\text{H}_2\text{O}$  and TEOA in the PHE reaction. ZMR-0.78 was coated on a glass slide to observe the phenomena of the PHE process, as shown in Fig. S31. Compared to the initial state, there was a continuous emergence of  $\text{H}_2$  bubbles from the surface of ZMR-0.78 under illumination. The PHE activity of  $\text{ZnIn}_2\text{S}_4$ -based photocatalysts decorated with precious metals under different actual qualities was compared. As shown in Fig. S32, the PHE activity of  $\text{ZnIn}_2\text{S}_4/\text{Mo}_2\text{TiC}_2\text{-Ru}$  is beyond the majority of representative photocatalysts, reaching a relatively high level. (specific parameters listed in Table S2).

The mechanism for the enhancement of PHE activity in  $\text{ZnIn}_2\text{S}_4/\text{Mo}_2\text{TiC}_2\text{-Ru}$  is shown in Fig. 5g. It can be seen that the PHE activity of  $\text{ZnIn}_2\text{S}_4$  is limited by the severe bulk carrier recombination and the sluggish surface reaction such as water dissociation and hydrogen adsorption.  $\text{Mo}_2\text{TiC}_2$  promotes the transfer of photogenerated electrons through electronic pathways and provides favorable hydrogen adsorption sites, yet its poor water dissociation ability still limits surface reactions. In contrast, the electron storage behavior of  $\text{Mo}_2\text{TiC}_2\text{-Ru}$  creates an electron-rich environment, which inhibits electron backflow and further promotes the spatial separation of photogenerated electrons. Meanwhile, the electron-rich environment constructed in “electron-parking” regulates the electronic structure of  $\text{Mo}_2\text{TiC}_2\text{-Ru}$ , synergistically accelerating the water dissociation and hydrogen adsorption kinetics, improving surface reaction rates. Therefore, the PHE activity of  $\text{ZnIn}_2\text{S}_4/\text{Mo}_2\text{TiC}_2\text{-Ru}$  under visible light irradiation is significantly increased compared to  $\text{ZnIn}_2\text{S}_4$  and  $\text{ZnIn}_2\text{S}_4/\text{Mo}_2\text{TiC}_2$ .

### 3.5. The electrons storage-release behavior of $\text{ZnIn}_2\text{S}_4/\text{Mo}_2\text{TiC}_2\text{-Ru}$

The electrons storage-release behavior of  $\text{ZnIn}_2\text{S}_4/\text{Mo}_2\text{TiC}_2\text{-Ru}$  was further investigated. The PHE activity of ZIS, ZM, and ZMR-0.78 under alternating light-dark conditions at intervals of 10 minutes is shown in Fig. 6a (blue region). As a control, their PHE activity under continuous 30-minute illumination was also tested (red region). The  $\text{Mo}_2\text{TiC}_2\text{-Ru}$  cocatalyst does not generate hydrogen under alternating light-dark and continuous irradiation conditions. After each illumination period, ZMR-0.78 immediately continues to sustain a certain rate of hydrogen evolution activity under dark conditions. The total PHE activity of ZMR-0.78 under light-dark alternating conditions (with a total illumination of 30 min) was significantly higher in comparison to the 30-minute continuous illumination condition, while the PHE activity of ZIS and ZM remained nearly unchanged in both conditions. Furthermore, Fig. 6b displays the PHE rates at 10-minute intervals for ZIS, ZM, and ZMR-0.78 under alternating light-dark alternating conditions. Under dark conditions, the average PHE rate of ZMR-0.78 is  $\sim 1.67\text{ mmol}\cdot\text{g}^{-1}\cdot\text{h}^{-1}$ , while the PHE rates of ZIS ( $\sim 0.17\text{ mmol}\cdot\text{g}^{-1}\cdot\text{h}^{-1}$ ) and ZM ( $\sim 0.32\text{ mmol}\cdot\text{g}^{-1}\cdot\text{h}^{-1}$ ) are significantly lower and almost negligible. The sustained PHE activity under alternating light-dark conditions reflects the storage of photogenerated electrons as “electron-parking” in the presence of light and is immediately released under dark conditions to continue the PHE reaction.

The capacitance values of  $\text{Mo}_2\text{TiC}_2\text{-Ru}$  were calculated using cyclic voltammetry curves at different scan rates (Fig. S33), as shown in Table S3. And Fig. S34 shows the cyclic voltammetry curves of  $\text{Mo}_2\text{TiC}_2$  and  $\text{Mo}_2\text{TiC}_2\text{-Ru}$  at a scan rate of 10 mV/s. As shown in Fig. 6c, the capacitance of  $\text{Mo}_2\text{TiC}_2\text{-Ru}$  exhibits a “volcano-shaped” trend with an initial increase followed by a decrease as the Ru loading increases, which is consistent with its role as a cocatalyst in enhancing the PHE activity of ZMR-0.78. The high capacitance value of  $\text{Mo}_2\text{TiC}_2\text{-Ru}$  may be attributed to the synergistic interaction between  $\text{Mo}_2\text{TiC}_2$  and Ru. The capacitance of MX-50 reaches a maximum value of 90.46 F/g, indicating its high electron storage capability. The non-rectangular CV curve of MR-50 (Fig. S35) shows an obvious redox peak, and the GCD test under different current densities (Fig. S36) exhibits a non-linear relationship in its potential-time curve, indicating that the pseudocapacitance of  $\text{Mo}_2\text{TiC}_2\text{-Ru}$  is predominantly driven by reversible redox or Faraday charge transfer reactions [60]. The EIS Nyquist plot (Fig. S37) shows that  $\text{Mo}_2\text{TiC}_2\text{-Ru}$  exhibits a smaller EIS semicircle diameter, indicating that the loading of Ru NPs significantly reduces the charge transfer resistance of  $\text{Mo}_2\text{TiC}_2\text{-Ru}$ , accelerating the electron conduction and rapid storage. Moreover, the capacitance values of ZIS, ZM, and ZMR-0.78 were calculated using cyclic voltammetry curves at different scan rates (Fig. S38), as shown in Table S4. And Fig. S39 displays the cyclic voltammetry curves of ZIS, ZM, and ZMR-0.78 at a scan rate of 10 mV/s. As observed in Fig. 6d, the PHE rate of ZIS, ZM, and ZMR-0.78 gradually increases with an increase in capacitance, indicating that the increase of capacitance plays a key role in improving the PHE performance. The above results demonstrate that the  $\text{Mo}_2\text{TiC}_2\text{-Ru}$  with larger capacitance, as the “electron-parking” in  $\text{ZnIn}_2\text{S}_4/\text{Mo}_2\text{TiC}_2\text{-Ru}$ , provides a favorable platform for the construction of electron-rich environment and the storage-release of electrons.

The electrons storage-release behavior in “electron parking” was further verified. Compared to the almost negligible drop of ZIS and ZM, the photoinduced potential in Fig. 6e of ZMR-0.78 did not immediately return to its initial state after the light off, validating the electron storage capability of ZMR-0.78 [61]. Another evidence for the stored electrons in “electron-parking” was obtained from quasi-in situ UV-vis DRS spectra (the full spectrum is shown in Fig. S40). The storage of photogenerated electrons leads to an increase in the optical absorption intensity of the material [62]. Fig. 6f shows that the absorption changes of ZIS and ZM under illumination are negligible, whereas the absorbance of ZMR-0.78 gradually increases with prolonged light exposure, confirming the storage and accumulation of photogenerated electrons from ZIS

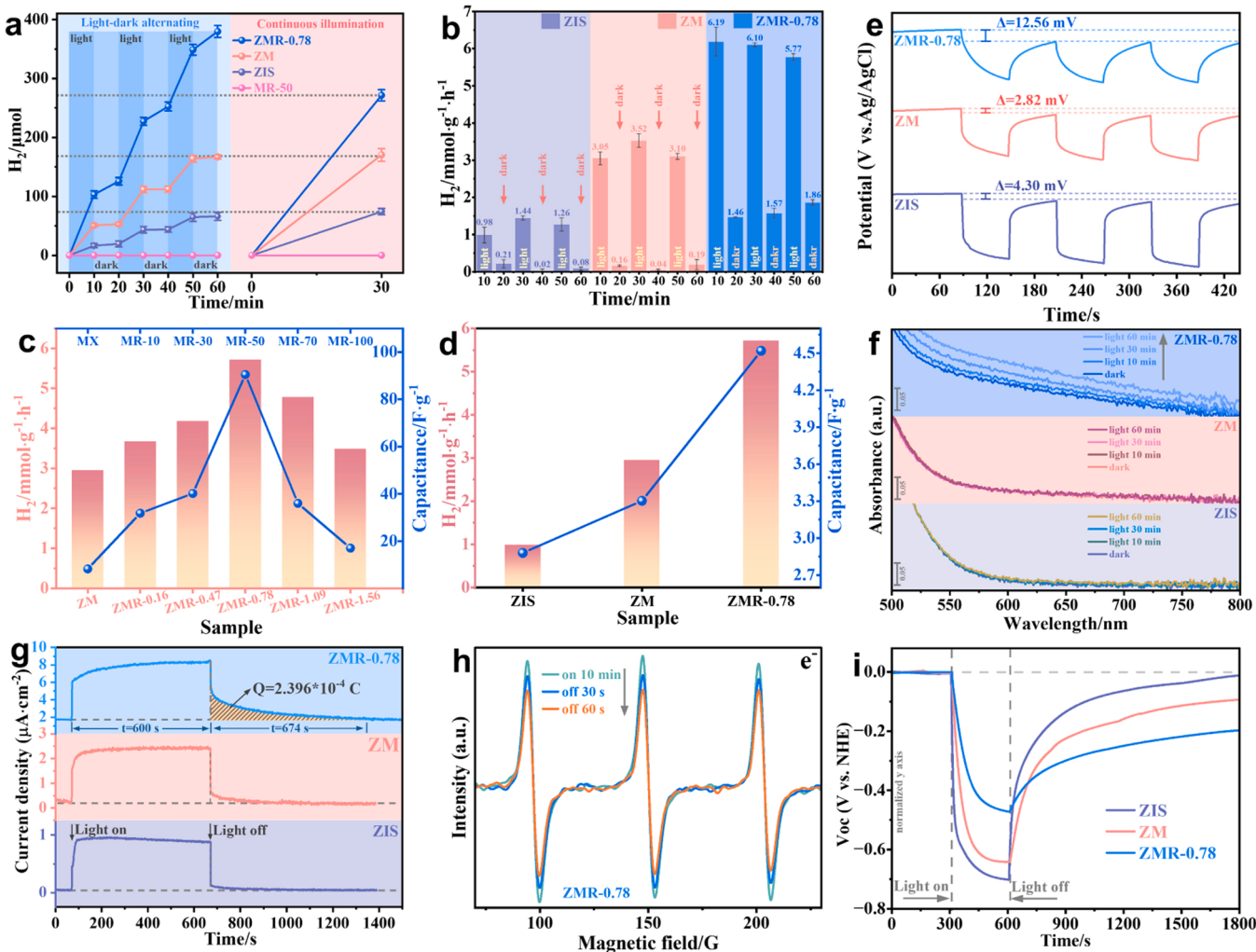


**Fig. 6.** (a) PHE activity of MR-50, ZIS, ZM, and ZMR-0.78 under light-dark and continuous light conditions. (b) PHE rate of ZIS, ZM, and ZMR-0.78 during the light-dark process. The experiments were repeated three times in parallel to calculate the average values and error bars. (c, d) Relationship between PHE rate and capacitance values of different samples. (e) Photoinduced potential of ZIS, ZM, and ZMR-0.78. (f) Quasi-in situ UV-vis diffuse reflectance spectrum of ZIS, ZM, and ZMR-0.78. (g) Current-time curves of ZIS, ZM, and ZMR-0.78 after 600 s of illumination. (h) EPR signal of the TEMPO-e<sup>-</sup> spin adduct spectrum of ZMR-0.78 under light-on/off condition. (i) Open-circuit voltage decay (OCVD) spectrum of ZIS, ZM, and ZMR-0.78.

to the  $\text{Mo}_2\text{TiC}_2\text{-Ru}$  “electron-parking”. Furthermore, the electron storage-release process of ZMR-0.78 is validated through the i-t curves, as shown in Fig. 6g. Within 600 seconds of illumination, the photoinduced current density of ZMR-0.78 continuously accumulates under illumination, attributed to the rapid transfer and storage of photo-generated electrons, result in an increased electron density. Subsequently, ZMR-0.78 exhibited a slow decrease in current density after the light off, and it could continuously release  $2.396 \times 10^{-4} \text{ C}$  of electrons for 674 seconds in the dark, indicating the excellent electron storage-release capability of ZMR-0.78 [63]. As controls, the photoinduced current densities of ZIS and ZM rapidly stabilize and almost instantly decreases upon light off, indicating the rapid recombination of photogenerated electrons, thereby verifying their lack of electron storage capacity. The in-situ EPR spectra of ZMR-0.78 were further tested. The generation of electrons is observed through the attenuation of the EPR signal of TEMPO-e<sup>-</sup> spin adduct, as electrons have the ability to reduce TEMPO to TEMPOH [64]. Fig. S41 demonstrates that ZMR-0.78 exhibits a substantially lower extent of EPR decay compared to ZIS after 10 min of illumination. This suggests that ZMR-0.78 can generate a higher number of photogenerated electrons, potentially attributed to the efficient transfer and storage of these electrons in  $\text{Mo}_2\text{TiC}_2\text{-Ru}$  “electron-parking”. As shown in Fig. 6h, the EPR signal of ZMR-0.78

continues to decay after the cessation of illumination, representing a continuous consumption of electrons. In comparison, the EPR signal of ZIS exhibits almost no decay (Fig. S42). Therefore, the above in-situ EPR results indicate that photogenerated electrons generated from ZIS can be transferred to  $\text{Mo}_2\text{TiC}_2\text{-Ru}$  “electron-parking” for storage and continued released after light off. The decay of OCVD was measured for ZIS, ZM, and ZMR-0.78. Light irradiation under open-circuit conditions causes the holes to be driven to the surface and consumed by the water oxidation, while the electrons are accumulated [3]. With continuous illumination, the accumulation and recombination of electrons gradually reach equilibrium [65]. In Fig. 6i, ZMR-0.78 exhibits a significantly slower decay after the light is turned off compared to ZIS and ZM, indicating that the photogenerated electrons in ZMR-0.78 can be stored in  $\text{Mo}_2\text{TiC}_2\text{-Ru}$  “electron-parking” and slowly released in the dark [66]. In addition, the electron lifetime ( $\tau_n$ ) calculated by OCVD reflects the rate at which the charge distribution state returns to the quasi-Fermi level after the termination of light irradiation [67]. In Fig. S43, the value of  $\tau_n$  for ZM-0.78 is one order of magnitude higher than that of ZIS and ZM, indicating a more sustained release of photogenerated electrons in the dark.

Based on the analysis and discussion above, the potential mechanism for the efficient and sustainable PHE activity of  $\text{ZnIn}_2\text{S}_4/\text{Mo}_2\text{TiC}_2\text{-Ru}$

based on the “electron-parking” strategy under light and dark conditions is illustrated in Fig. 7. Under the stimulation of light, photogenerated electron “cars” continuously emanate from the ZIS “station”.  $\text{Mo}_2\text{TiC}_2$  facilitates the transfer of photogenerated electrons and offers favorable HER sites, but its poor water dissociation results in limited enhancement of PHE performance. In contrast,  $\text{Mo}_2\text{TiC}_2\text{-Ru}$  with “electron-parking” stores photogenerated electrons from ZIS, creating an electron-rich environment that not only further promotes the spatial separation of photogenerated electrons, but also synergistically optimizes the surface water dissociation and hydrogen release reactions kinetics. More importantly, the electrons stored in the “electron parking” of  $\text{Mo}_2\text{TiC}_2\text{-Ru}$  continue to be released in dark conditions for the PHE reaction, significantly alleviating the issue of  $\text{ZnIn}_2\text{S}_4$  being unable to provide photogenerated electrons due to its photodependence. Therefore, the electron storage-release behavior of  $\text{ZnIn}_2\text{S}_4/\text{Mo}_2\text{TiC}_2\text{-Ru}$  based on the “electron-parking” strategy enhances the electron utilization efficiency under intermittent sunlight, achieving sustained PHE performance.

#### 4. Conclusions

In summary, a  $\text{ZnIn}_2\text{S}_4/\text{Mo}_2\text{TiC}_2\text{-Ru}$  photocatalyst with “electron-parking” strategy was designed through the introduction of capacitive cocatalyst  $\text{Mo}_2\text{TiC}_2\text{-Ru}$ . Experiment combined with theoretical results show that  $\text{Mo}_2\text{TiC}_2\text{-Ru}$  “electron-parking” can store transferred electrons to form an electron-rich environment, which not only inhibits the electron backflow and promotes the transfer and separation of photogenerated electrons, but also accelerates the water dissociation and hydrogen release reactions kinetics through electronic structure regulation. Consequently,  $\text{ZnIn}_2\text{S}_4/\text{Mo}_2\text{TiC}_2\text{-Ru}$  exhibited significantly

enhanced PHE activity under irradiation, reaching  $5.72 \text{ mmol}\cdot\text{g}^{-1}\cdot\text{h}^{-1}$ . In addition, the stored photogenerated electrons could be released under dark conditions to continue the PHE reaction with a PHE activity of  $\sim 1.67 \text{ mmol}\cdot\text{g}^{-1}\cdot\text{h}^{-1}$ , indicating the effective utilization of the stored non-backflow electrons and the continuous PHE under intermittent light conditions. This study extensively investigated the multifaceted promotional effect of  $\text{Mo}_2\text{TiC}_2\text{-Ru}$  capacitive co-catalyst with “electron-parking” characteristics on PHE performance, providing valuable insights and considerations for the design of photocatalytic systems with efficient and sustainable PHE performance.

#### CRediT authorship contribution statement

**Jiancheng Wang:** Supervision, Resources, Formal analysis, Conceptualization. **Rui Li:** Writing – review & editing, Resources, Methodology, Data curation, Conceptualization. **Jun Ren:** Resources, Methodology. **Qing Xi:** Writing – review & editing, Writing – original draft, Investigation, Formal analysis, Conceptualization. **Caiwei Fan:** Supervision, Resources, Funding acquisition, Conceptualization. **Xiaoming Gao:** Software, Resources. **Yawen Wang:** Project administration, Funding acquisition. **Xiaochao Zhang:** Supervision, Methodology. **Houfen Li:** Supervision, Investigation. **Aijuan Zhou:** Supervision, Data curation. **Xuan Jian:** Methodology, Data curation. **Aoqun Jian:** Software, Resources. **Zijun Sun:** Software, Investigation. **Jianxin Liu:** Resources, Data curation. **Fangxia Xie:** Software, Investigation.

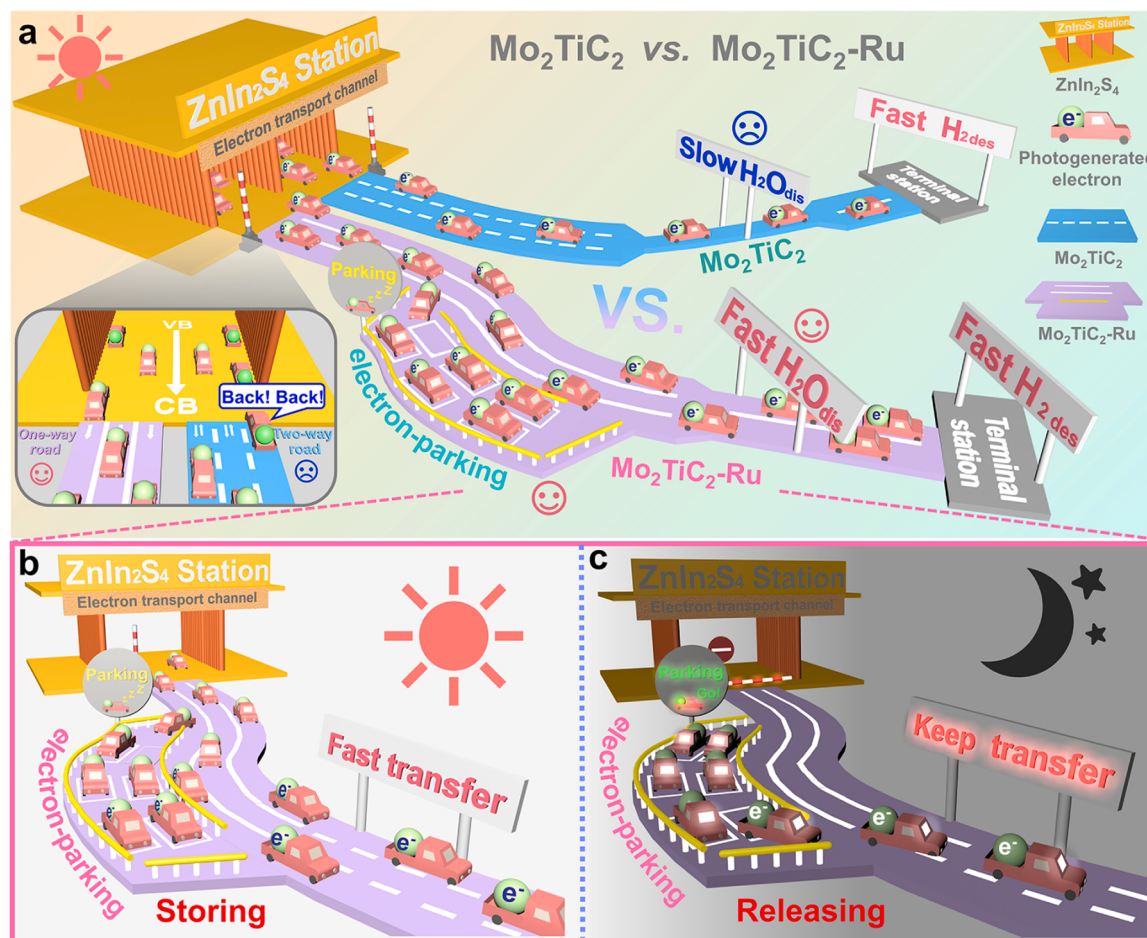


Fig. 7. The potential mechanism for the efficient and sustainable PHE activity of  $\text{ZnIn}_2\text{S}_4/\text{Mo}_2\text{TiC}_2\text{-Ru}$ .

## Declaration of Competing Interest

The authors declare that they have no known competing financial interests or personal relationships that could have appeared to influence the work reported in this paper.

## Data availability

Data will be made available on request.

## Acknowledgements

This work is financially supported by the Central Government Guides the Special Fund Projects of Local Scientific and Technological Development (YDZJSX20231A014), National Natural Science Foundation of China (No. 22008167), China Postdoctoral Science Foundation (No. 2022M712342), and Fundamental Research Program of Shanxi Province (No. 202203021221058, 202303021211031).

## Appendix A. Supporting information

Supplementary data associated with this article can be found in the online version at [doi:10.1016/j.apcatb.2024.124184](https://doi.org/10.1016/j.apcatb.2024.124184).

## References

- [1] L. Dai, A. Dong, X. Meng, H. Liu, Y. Li, P. Li, B. Wang, Enhancement of visible-light-driven hydrogen evolution activity of 2D π-conjugated bipyridine-based covalent organic frameworks via post-protonation, *Angew. Chem., Int. Ed.* 62 (2023) e202300224.
- [2] M. Xiao, B. Luo, S. Wang, L. Wang, Solar energy conversion on g-C<sub>3</sub>N<sub>4</sub> photocatalyst: light harvesting, charge separation, and surface kinetics, *J. Energy Chem.* 27 (2018) 1111–1123.
- [3] Q. Ruan, X. Xi, B. Yan, L. Kong, C. Jiang, J. Tang, Z. Sun, Stored photoelectrons in a faradaic junction for decoupled solar hydrogen production in the dark, *Chem* 9 (2023) 1850–1864.
- [4] S. Zhang, P. Du, H. Xiao, Z. Wang, R. Zhang, W. Luo, J. An, Y. Gao, B. Lu, Fast interfacial carrier dynamics modulated by bidirectional charge transport channels in ZnIn<sub>2</sub>S<sub>4</sub>-based composite photoanodes probed by scanning photoelectrochemical microscopy, *Angew. Chem., Int. Ed.* 63 (2023) e202315763.
- [5] J. Schneider, M. Matsuoka, M. Takeuchi, J. Zhang, Y. Horiuchi, M. Anpo, D. W. Bahnemann, Understanding TiO<sub>2</sub> photocatalysis: mechanisms and materials, *Chem. Rev.* 114 (2014) 9919–9986.
- [6] T. Ge, J. Chen, Evaluating a second time scale for hole extraction in an actual photocatalytic reaction: the method, *J. Phys. Chem. Lett.* 14 (2023) 7477–7482.
- [7] G.Z.S. Ling, S.-F. Ng, W.-J. Ong, Tailor-engineered 2D cocatalysts: harnessing electron-hole redox center of 2D g-C<sub>3</sub>N<sub>4</sub> photocatalysts toward solar-to-chemical conversion and environmental purification, *Adv. Funct. Mater.* 32 (2022) 2111875.
- [8] S. Zhang, J. Xu, H. Cheng, C. Zang, F. Bian, B. Sun, Y. Shen, H. Jiang, Photocatalytic H<sub>2</sub> evolution from ammonia borane: improvement of charge separation and directional charge transmission, *ChemSusChem* 13 (2020) 5264–5272.
- [9] Q. Jiang, N. Kurra, M. Alhabeb, Y. Gogotsi, H.N. Alshareef, All pseudocapacitive MXene-RuO<sub>2</sub> asymmetric supercapacitors, *Adv. Energy Mater.* 8 (2018) 1703043.
- [10] K. Khan, A.K. Tareen, M. Iqbal, I. Hussain, A. Mahmood, U. Khan, M.F. Khan, H. Zhang, Z. Xie, Recent advances in MXenes: a future of nanotechnologies, *J. Mater. Chem. A* 11 (2023) 19764–19811.
- [11] M.K. Aslam, Y. Niu, M. Xu, MXenes for non-lithium-ion (Na, K, Ca, Mg, and Al) batteries and supercapacitors, *Adv. Energy Mater.* 11 (2021) 2000681.
- [12] M. Pandey, K. Deshmukh, A. Raman, A. Asok, S. Appukuttan, G.R. Suman, Prospects of MXene and graphene for energy storage and conversion, *Renew. Sust. Energ. Rev.* 189 (2024) 114030.
- [13] Y. Guo, Z. Li, Y. Xia, Y. Wei, J. Zhang, Y. Wang, H. He, Facile SYNthesis of Ruthenium Nanoparticles Capped by Graphene and Thiols for High-performance Supercapacitors, *Electrochim. Acta* 391 (2021) 138990.
- [14] L. Zheng, G. Zhang, M. Zhang, S. Guo, Z.H. Liu, Preparation and capacitance performance of Ag-graphene based nanocomposite, *J. Power Sources* 201 (2012) 376–381.
- [15] X. Zheng, Y. Song, Y. Liu, Y. Yang, D. Wu, Y. Yang, S. Feng, J. Li, W. Liu, Y. Shen, X. Tian, ZnIn<sub>2</sub>S<sub>4</sub>-based photocatalysts for photocatalytic hydrogen evolution via water splitting, *Coord. Chem. Rev.* 475 (2023) 214898.
- [16] G. Zuo, Y. Wang, W.L. Teo, A. Xie, Y. Guo, Y. Dai, W. Zhou, D. Jana, Q. Xian, W. Dong, Y. Zhao, Ultrathin ZnIn<sub>2</sub>S<sub>4</sub> nanosheets anchored on Ti<sub>3</sub>C<sub>2</sub>T<sub>x</sub> MXene for photocatalytic H<sub>2</sub> evolution, *Angew. Chem., Int. Ed.* 59 (2020) 11287–11292.
- [17] M. Xu, X. Ruan, D. Meng, G. Fang, D. Jiao, S. Zhao, Z. Liu, Z. Jiang, K. Ba, T. Xie, W. Zhang, J. Leng, S. Jin, S. Ravi, X. Cui, Modulation of sulfur vacancies in ZnIn<sub>2</sub>S<sub>4</sub>/MXene schottky heterojunction photocatalyst promotes hydrogen evolution, *Adv. Funct. Mater.* (2024) 2402330.
- [18] S. Li, L. Shao, Z. Yang, S. Cheng, C. Yang, Y. Liu, X. Xia, Constructing Ti<sub>3</sub>C<sub>2</sub> MXene/ZnIn<sub>2</sub>S<sub>4</sub> heterostructure as a schottky catalyst for photocatalytic environmental remediation, *Green Energy Environ.* 7 (2022) 246–256.
- [19] Q. Xi, F. Xie, J. Liu, X. Zhang, J. Wang, Y. Wang, Y. Wang, H. Li, Z. Yu, Z. Sun, X. Jian, X. Gao, J. Ren, C. Fan, R. Li, In situ formation ZnIn<sub>2</sub>S<sub>4</sub>/Mo<sub>2</sub>TiC<sub>2</sub> schottky junction for accelerating photocatalytic hydrogen evolution kinetics: manipulation of local coordination and electronic structure, *Small* 19 (2023) 2300717.
- [20] J. Li, Y. Li, J. Wang, C. Zhang, H. Ma, C. Zhu, D. Fan, Z. Guo, M. Xu, Y. Wang, H. Ma, Elucidating the critical role of ruthenium single atom sites in water dissociation and dehydrogenation behaviors for robust hydrazine oxidation-boosted alkaline hydrogen evolution, *Adv. Funct. Mater.* 32 (2022) 2109439.
- [21] F. Zhou, Y. Zhang, J. Wu, W. Yang, X. Fang, T. Jia, Y. Ling, P. He, Q. Liu, J. Lin, Utilizing Er-doped ZnIn<sub>2</sub>S<sub>4</sub> for efficient photocatalytic CO<sub>2</sub> conversion, *Appl. Catal., B*, 341 (2024) 123347.
- [22] J. Zhang, Y. Zhao, X. Guo, C. Chen, C.-L. Dong, R.-S. Liu, C.-P. Han, Y. Li, Y. Gogotsi, G. Wang, Single atoms immobilized on an MXene as an efficient catalyst for the hydrogen evolution reaction, *Nat. Catal.* 1 (2018) 985–992.
- [23] T. Luo, J. Huang, Y. Hu, C. Yuan, J. Chen, L. Cao, K. Kajiyoshi, Y. Liu, Y. Zhao, Z. Li, Y. Feng, Fullerene lattice-confined Ru nanoparticles and single atoms synergistically boost electrocatalytic hydrogen evolution reaction, *Adv. Funct. Mater.* 33 (2023) 2213058.
- [24] X. Shi, C. Dai, X. Wang, J. Hu, J. Zhang, L. Zheng, L. Mao, H. Zheng, M. Zhu, Protruding Pt single-sites on hexagonal ZnIn<sub>2</sub>S<sub>4</sub> to accelerate photocatalytic hydrogen evolution, *Nat. Commun.* 13 (2022) 1287.
- [25] J.-Y. Li, Y.-H. Li, F. Zhang, Z.-R. Tang, Y.-J. Xu, Visible-light-driven integrated organic synthesis and hydrogen evolution over 1D/2D CdS-Ti<sub>3</sub>C<sub>2</sub>T<sub>x</sub> MXene composites, *Appl. Catal., B*, 269 (2020) 118783.
- [26] G. Peng, J.E. Ellis, G. Xu, X. Xu, A. Star, In situ grown TiO<sub>2</sub> nanospindles facilitate the formation of holey reduced graphene oxide by photodegradation, *ACS Appl. Mater. Interfaces* 8 (2016) 7403–7410.
- [27] C. Yang, Q. Tan, Q. Li, J. Zhou, J. Fan, B. Li, J. Sun, K. Lv, 2D/2D Ti<sub>3</sub>C<sub>2</sub> MXene/g-C<sub>3</sub>N<sub>4</sub> nanosheets heterojunction for high efficient CO<sub>2</sub> reduction photocatalyst: dual effects of urea, *Appl. Catal., B*, 268 (2020) 118738.
- [28] Z. Liu, Y. Lu, M.P. Confer, H. Cui, J. Li, Y. Li, Y. Wang, S.C. Street, E.K. Wujcik, R. Wang, Thermally stable RuO<sub>x</sub>-CeO<sub>2</sub> nanofiber catalysts for low-temperature CO oxidation, *ACS Appl. Nano. Mater.* 3 (2020) 8403–8413.
- [29] X. Wang, L. Li, Z. Fang, Y. Zhang, J. Ni, B. Lin, L. Zheng, C.-t. Au, L. Jiang, Atomically dispersed Ru catalyst for low-temperature nitrogen activation to ammonia via an associative mechanism, *ACS Catal.* 10 (2020) 9504–9514.
- [30] K. Sato, S. Zaitsu, G. Kitayama, S. Yagi, Y. Kayada, Y. Nishida, Y. Wada, K. Nagaoka, Operando spectroscopic study of the dynamics of Ru catalyst during preferential oxidation of CO and the prevention of ammonia poisoning by Pt, *JACS Au* 2 (2022) 1627–1637.
- [31] T. Nakamura, M.-a Ohshima, H. Kurokawa, H. Miura, Effects of removing residual chlorine on the hydrogenation of aromatic hydrocarbons over supported Ru catalysts, *Chem. Lett.* 39 (2009) 62–63.
- [32] P. Panagiotopoulou, D.I. Kondarides, X.E. Verykios, Mechanistic study of the selective methanation of CO over Ru/TiO<sub>2</sub> catalyst: identification of active surface species and reaction pathways, *J. Phys. Chem. C* 115 (2011) 1220–1230.
- [33] B. Lu, L. Guo, F. Wu, Y. Peng, J.E. Lu, T.J. Smart, N. Wang, Y.Z. Finfrock, D. Morris, P. Zhang, N. Li, P. Gao, Y. Ping, S. Chen, Ruthenium atomically dispersed in carbon outperforms platinum toward hydrogen evolution in alkaline media, *Nat. Commun.* 10 (2019) 631.
- [34] X. Dang, M. Xie, F. Dai, J. Guo, J. Liu, X. Lu, Ultrathin 2D/2D ZnIn<sub>2</sub>S<sub>4</sub>/g-C<sub>3</sub>N<sub>4</sub> nanosheet heterojunction with atomic-level intimate interface for photocatalytic hydrogen evolution under visible light, *Adv. Mater. Interfaces* 8 (2021) 2100151.
- [35] K. Huang, C. Li, X. Meng, In-situ construction of ternary Ti<sub>3</sub>C<sub>2</sub> MXene@TiO<sub>2</sub>/ZnIn<sub>2</sub>S<sub>4</sub> composites for highly efficient photocatalytic, *Hydrog. Evol. J. Colloid Interf. Sci.* 580 (2020) 669–680.
- [36] T. Ni, Z. Yang, Y. Cao, H. Lv, Y. Liu, Rational design of MoS<sub>2</sub>/g-C<sub>3</sub>N<sub>4</sub>/ZnIn<sub>2</sub>S<sub>4</sub> hierarchical heterostructures with efficient charge transfer for significantly enhanced photocatalytic H<sub>2</sub> production, *Ceram. Int.* 47 (2021) 22985–22993.
- [37] Z. Zhuang, Y. Li, Z. Li, F. Lv, Z. Lang, K. Zhao, L. Zhou, L. Moskaleva, S. Guo, L. Mai, MoB/g-C<sub>3</sub>N<sub>4</sub> interface materials as a schottky catalyst to boost hydrogen evolution, *Angew. Chem., Int. Ed.* 57 (2018) 496–500.
- [38] P. Su, W. Pei, X. Wang, Y. Ma, Q. Jiang, J. Liang, S. Zhou, J. Zhao, J. Liu, G.Q. Lu, Exceptional electrochemical HER performance with enhanced electron transfer between Ru nanoparticles and single atoms dispersed on a carbon substrate, *Angew. Chem., Int. Ed.* 60 (2021) 16044–16050.
- [39] X. Wang, X. Yang, G. Pei, J. Yang, J. Liu, F. Zhao, F. Jin, W. Jiang, H. Ben, L. Zhang, Strong metal-support interaction boosts the electrocatalytic hydrogen evolution capability of Ru nanoparticles supported on titanium nitride, *Carbon Energy* (2023) e391 (n/a).
- [40] X. Zheng, L. Feng, Y. Dou, H. Guo, Y. Liang, G. Li, J. He, P. Liu, J. He, High carrier separation efficiency in morphology-controlled BiOBr/C schottky junctions for photocatalytic overall water splitting, *ACS Nano* 15 (2021) 13209–13219.
- [41] F. Meng, S.K. Cushing, J. Li, S. Hao, N. Wu, Enhancement of solar hydrogen generation by synergistic interaction of La<sub>2</sub>Ti<sub>2</sub>O<sub>7</sub> photocatalyst with plasmonic gold nanoparticles and reduced graphene oxide nanosheets, *ACS Catal.* 5 (2015) 1949–1955.
- [42] D. Lancet, I. Pecht, Spectroscopic and immunochemical studies with nitrobenzoxadiazolealanine, A fluorescent dinitrophenyl analog, *Biochemistry* 16 (1977) 5150–5157.
- [43] X. Cai, Z. Zeng, Y. Liu, Z. Li, X. Gu, Y. Zhao, L. Mao, J. Zhang, Visible-light-driven water splitting by yolk-shelled ZnIn<sub>2</sub>S<sub>4</sub>-based heterostructure without noble-metal Co-catalyst and sacrificial agent, *Appl. Catal., B*, 297 (2021) 120391.

- [44] R. Li, J. Liu, X. Zhang, Y. Wang, Y. Wang, C. Zhang, X. Zhang, C. Fan, Iodide-modified  $\text{Bi}_2\text{O}_5\text{Br}_2$  photocatalyst with tunable conduction band position for efficient visible-light decontamination of pollutants, *Chem. Eng. J.* 339 (2018) 42–50.
- [45] H. Dong, L. Tong, P. Zhang, D. Zhu, J. Jiang, C. Li, Built-in electric field intensified by photothermoelectric effect drives charge separation over Z-scheme 3D/2D  $\text{In}_2\text{Se}_3/\text{PCN}$  heterojunction for high-efficiency photocatalytic  $\text{CO}_2$  reduction, *J. Mater. Sci. Technol.* 179 (2024) 251–261.
- [46] X. Chen, J. Wang, Y. Chai, Z. Zhang, Y. Zhu, Efficient photocatalytic overall water splitting induced by the giant internal electric field of a g-C<sub>3</sub>N<sub>4</sub>/rGO/PDIP Z-scheme heterojunction, *Adv. Mater.* 33 (2021) 2007479.
- [47] Y. Zhao, P. Zhang, Z. Yang, L. Li, J. Gao, S. Chen, T. Xie, C. Diao, S. Xi, B. Xiao, C. Hu, W. Choi, Mechanistic analysis of multiple processes controlling solar-driven  $\text{H}_2\text{O}_2$  synthesis using engineered polymeric carbon nitride, *Nat. Commun.* 12 (2021) 3701.
- [48] R. Li, F. Xie, J. Liu, C. Zhang, X. Zhang, C. Fan, Room-temperature hydrolysis fabrication of  $\text{BiOBr}/\text{Bi}_{12}\text{O}_{17}\text{Br}_2$  Z-scheme photocatalyst with enhanced resorcinol degradation and NO removal activity, *Chemosphere* 235 (2019) 767–775.
- [49] C. Li, N. Su, H. Wu, C. Liu, G. Che, H. Dong, Synergies of adjacent sites in atomically dispersed ruthenium toward achieving stable hydrogen evolution, *Inorg. Chem.* 61 (2022) 13453–13461.
- [50] C. Li, P. Zhang, F. Gu, L. Tong, J. Jiang, Y. Zuo, H. Dong, Atomically dispersed Au confined by oxygen vacancies in  $\text{Au}-\theta\text{-Al}_2\text{O}_3/\text{Au}/\text{PCN}$  hybrid for boosting photocatalytic  $\text{CO}_2$  reduction driven by multiple built-in electric fields, *Chem. Eng. J.* 476 (2023) 146514.
- [51] Z. Shen, F. Li, L. Guo, X. Zhang, Y. Wang, Y. Wang, X. Jian, X. Gao, Z. Wang, R. Li, C. Fan, J. Liu, Ligand bridged MXene/metal organic frameworks heterojunction for efficient photocatalytic ammonia synthesis, *Appl. Catal., B.* 346 (2024) 123732.
- [52] F. Xie, Q. Xi, H. Li, X. Jian, J. Liu, X. Zhang, Y. Wang, R. Li, C. Fan, Two-dimensional/two-dimensional heterojunction-induced accelerated charge transfer for photocatalytic hydrogen evolution over  $\text{Bi}_5\text{O}_3\text{Br}/\text{Ti}_3\text{C}_2$ : electronic directional transport, *J. Colloid Interf. Sci.* 617 (2022) 53–64.
- [53] P. Zhang, H. Cheng, F. Gu, S. Hong, H. Dong, C. Li, Progress on iron-series metal-organic frameworks materials towards electrocatalytic hydrogen evolution reaction, *Surf. Interfaces* 42 (2023) 103368.
- [54] Y. Jiang, Y.-P. Deng, R. Liang, J. Fu, R. Gao, D. Luo, Z. Bai, Y. Hu, A. Yu, Z. Chen, D-orbital steered active sites through ligand editing on heterometal imidazole frameworks for rechargeable zinc-air battery, *Nat. Commun.* 11 (2020) 5858.
- [55] L. Wu, F. Zhang, S. Song, M. Ning, Q. Zhu, J. Zhou, G. Gao, Z. Chen, Q. Zhou, X. Xing, T. Tong, Y. Yao, J. Bao, L. Yu, S. Chen, Z. Ren, Efficient alkaline water/seawater hydrogen evolution by a nanorod-nanoparticle-structured Ni-MoN catalyst with fast water-dissociation kinetics, *Adv. Mater.* 34 (2022) 2201774.
- [56] Q. Dai, L. Wang, K. Wang, X. Sang, Z. Li, B. Yang, J. Chen, L. Lei, L. Dai, Y. Hou, Accelerated water dissociation kinetics by electron-enriched cobalt sites for efficient alkaline hydrogen evolution, *Adv. Funct. Mater.* 32 (2022) 2109556.
- [57] J. Wei, M. Zhou, A. Long, Y. Xue, H. Liao, C. Wei, Z.J. Xu, Heterostructured electrocatalysts for hydrogen evolution reaction under alkaline conditions, *Nano-Micro Lett.* 10 (2018) 75.
- [58] S. Cao, L. Piao, Considerations for a more accurate evaluation method for photocatalytic water splitting, *Angew. Chem., Int. Ed.* 59 (2020) 18312–18320.
- [59] C. Bie, B. Zhu, L. Wang, H. Yu, C. Jiang, T. Chen, J. Yu, A. Bifunctional,  $\text{CdS}/\text{MoO}_2/\text{MoS}_2$  catalyst enhances photocatalytic  $\text{H}_2$  evolution and pyruvic acid synthesis, *Angew. Chem., Int. Ed.* 61 (2022) e202212045.
- [60] J. Zhang, J. Zheng, W. Yang, Green supercapacitor assisted photocatalytic fuel cell system for sustainable hydrogen production, *Chem. Eng. J.* 403 (2021) 126368.
- [61] Y. Yang, M. Sun, Z. Chen, H. Xu, X. Wang, J. Duan, B. Hou, 3D nanothorn cluster-Like  $\text{Zn}-\text{Bi}_2\text{S}_3$  sensitized  $\text{WO}_3/\text{ZnO}$  multijunction with electron-storage characteristic and adjustable energy band for improving sustained photoinduced cathodic protection application, *Chem. Eng. J.* 458 (2023) 141458.
- [62] Y. Choi, M.S. Koo, A.D. Bokare, D.-h Kim, D.W. Bahnemann, W. Choi, Sequential process combination of photocatalytic oxidation and dark reduction for the removal of organic pollutants and Cr(VI) using Ag/TiO<sub>2</sub>, *Environ. Sci. Technol.* 51 (2017) 3973–3981.
- [63] J. Tian, F. Qian, M. Cao, J. Gong, J. Li, L. Wang, M. Tian, Z. Chen, A. Mo, Doping  $\text{WO}_3/\text{CdZnS}$  heterojunction photoelectrode for boosting electron storage capacity, *Appl. Surf. Sci.* 634 (2023) 157680.
- [64] Q. Gao, J. Li, B. Liu, C. Liu, In-situ synthesis of direct Z-scheme 2D/2D  $\text{ZnIn}_2\text{S}_4@\text{CeO}_2$  heterostructure toward enhanced photodegradation and Cr(VI) reduction, *J. Alloy. Compd.* 931 (2023) 167430.
- [65] B. Sun, T. Shi, X. Tan, Z. Liu, Y. Wu, G. Liao, Iridium oxide modified CdSe/CdS/TiO<sub>2</sub> nanorods for efficient and stable photoelectrochemical water splitting, *Mater. Today.: Proc.* 3 (2016) 443–448.
- [66] X. Sun, G. Liu, X. Xu, Defect management and efficient photocatalytic water oxidation reaction over Mg modified  $\text{SrNbO}_2\text{N}$ , *J. Mater. Chem. A.* 6 (2018) 10947–10957.
- [67] Y. Chen, Z. Wang, Y. Zhang, P. Wei, W. Xu, H. Wang, H. Yu, J. Jia, K. Zhang, C. Peng, S-scheme and schottky junction synchronous regulation boost hierarchical  $\text{CdS}@\text{Nb}_2\text{O}_5/\text{Nb}_2\text{CT}_x$  (MXene) heterojunction for photocatalytic  $\text{H}_2$  production, *ACS Appl. Mater. Interfaces* 15 (2023) 20027–20039.